Chemical Engineering Journal 428 (2022) 131155

Contents lists available at ScienceDirect

Chemical Engineering Journal

journal homepage: www.elsevier.com/locate/cej

A multifunctional antibacterial coating on bone implants for osteosarcoma therapy and enhanced osteointegration

Guannan Zhang [a,1], Zhuangzhuang Wu [b,1], Yongqiang Yang [c], Jing Shi [d], Jia Lv [b], Yi Fang [b], Zhen Shen [b], Zhi Lv [b,*], Pengcui Li [b], Xiaohong Yao [a], Weiyi Chen [e], Xiaochun Wei [b], Paul K. Chu [f], Xiangyu Zhang [a,b,e,*]

[a] Laboratory of Biomaterial Surfaces & Interfaces, College of Materials Science and Engineering, Taiyuan University of Technology, Taiyuan 030024, China
[b] Shanxi Key Laboratory of Bone and Soft Tissue Injury Repair, Department of Orthopedics, Second Hospital of Shanxi Medical University, Taiyuan 030024, China
[c] Jiangsu Provinces Special Equipment Safety Supervision Inspection Institute, Branch of Wuxi, National Graphene Products Quality Supervision and Inspection Center, Jiangsu, Wuxi 214174, PR China
[d] Analytical Instrumentation Center, State Key Laboratory of Coal Conversion, Institute of Coal Chemistry, Chinese Academy of Sciences, Taiyuan 030001, China
[e] College of Biomedical Engineering, Taiyuan University of Technology, Taiyuan 030024, China
[f] Department of Physics, Department of Materials Science and Engineering, Department of Biomedical Engineering, City University of Hong Kong, Tat Chee Avenue, Kowloon, Hong Kong, China

ARTICLE INFO

Keywords:
Multifunctional coating
Light-assisted therapy
Osteosarcoma
Antibiofilm
Osseointegration

ABSTRACT

After prosthesis replacement for the treatment of bone tumors, incomplete removal of tumor cells is the main challenge. Moreover, combating implant-associated infection and simultaneously promoting osseointegration are highly demanded for orthopedic implants and therefore, a multifunctional coating that produces tumor therapeutic effects, antibacterial activity, and osteogenesis at the same time is of clinical significance. Herein, a phototherapy platform composed of rare-earth elements - doped titanium dioxide nano-shovel/quercetin/L-arginine (TiO_2@UCN/Qr/LA) on titanium bone implant is fabricated. The stable nano-shovel structure prepared by a hydrothermal method improves the photothermal conversion ability of titanium. Incorporation of Yb and Er enhances the upconversion capability, thereby facilitating generation of reactive oxygen species (ROS) during exposure to near-infrared II (NIR-II) light. Furthermore, under the action of ROS, L-arginine is catalyzed to release nitric oxide (NO) free radicals. *In vitro* and *in vivo* experiments indicate that the combined actions of ROS, quercetin, and NO not only inhibit bone tumor growth at a temperature of 48 ℃, but also eliminate *Staphylococcus aureus* biofilms on the Ti implants at a mild temperature of 45 ℃ upon illumination with a 1,060 nm laser. Moreover, TiO_2@UCN/Qr/LA promotes angiogenesis and osteogenic differentiation, reduces inflammation, and accelerates formation of new bone tissues.

1. Introduction

Osteosarcoma is an aggressive malignant tumor occurring mainly in children and adolescents [1–5]. The common treatment strategy is surgery and some patients also need prosthesis replacements [6–8]. However, incomplete obliteration of tumor cells is frequently observed after surgery [9,10,11,12] and poor osseointegration and infection caused by biofilms often prolong the healing time risking amputation [13–15]. Therefore, implants should possess multiple functions including elimination of residual tumor cells, enhanced osseointegration, and bacteria resistance. Yuan et al. prepared a multifunctional MoS_2/PDA-RGD coating which not only improved the osteogenesis of MSCs, but also endowed Ti implant with antibacterial ability when exposing to NIR (808 nm) laser [16]. Xiang et al prepared a DTC@BG scaffold which can be used for photothermal ablation of bone tumors and stimulation of newborn bone formation [17]. Unfortunately, very few biomedical implants possess all three properties inherently and so development of the suitable multifunctional coatings is of clinical interest albeit challenging.

Near-infrared (NIR) light - assisted therapy including photothermal

* Corresponding authors.
E-mail addresses: zhilv2013@163.com (Z. Lv), zhangxiangyu@tyut.edu.cn (X. Zhang).
[1] These authors contributed equally

https://doi.org/10.1016/j.cej.2021.131155
Received 5 May 2021; Received in revised form 25 June 2021; Accepted 1 July 2021
Available online 7 July 2021

therapy (PTT) and photodynamic therapy (PDT) is a useful cancer therapy [18–20]. NIR-II light can penetrate tissues more deeply than NIR-I light because of weaker absorption by interstitial fluids, fats, and skin tissues and hence, NIR-II light - assisted therapy has large clinical potential [21,22]. PTT has also been demonstrated to not only obliterate tumor tissues, but also kill bacteria [23,24]. However, the single PTT treatment typically requires a relatively high temperature to eliminate tumors and bacterial biofilms resulting in scalding of surrounding normal tissues [25]. Similarly, when PDT is applied alone, the excess amount of ROS can produce deleterious effects in the human body [26,25]. However, when PTT and PDT are implemented in concert, the synergistic effects have been shown to kill tumor cells and bacteria at the same time with a relatively small amounts of ROS and low temperature [27,26].

With the development of nanotechnology, gas-generating nanoplatforms (GGNs) have desirable therapeutic features [28–30]. Nitric oxide (NO) which affects many physiological processes such as angiogenesis, immune response, and bone transduction is used in anti-tumor treatment, anti-biofilm formation, stem cell therapy, and angiogenesis [31–34]. Generally, a high concentration of NO ($10^{-3} \sim 10^{-6}$ M) can kill cancer cells directly *via* interactions with mitochondria and DNA [35,36] and moreover, NO can enter bacteria to inhibit growth [37,38]. Low concentrations of NO ($10^{-9} \sim 10^{-12}$ M) accelerate vascular remodeling and production because of regulation of proliferation and migration of endothelial cells through the physiological effects of extracellular signals [39,40]. NO has also been shown to be an auxiliary modality to improve the therapeutic effects of PTT or PDT [41,42]. However, NO must be released precisely and controllably to the diseased area - in the treatment but the small diffusion range and short half-life of NO are limitations in clinical applications [43,44]. L-Arginine (LA) as a NO donor can produce NO *via* catalysis of NO synthase (NOS) or ROS and good biocompatibility has been demonstrated [45,46].

Herein, a multifunctional coating which can be triggered by NIR-II light is designed and fabricated on Ti implants to achieve bone tumor treatment, anti-biofilm formation, as well as osseointegration simultaneously. The stable TiO_2 nano-shovel arrays are formed on the Ti implants by hydrothermal in tetramethylammonium hydroxide (TMAOH), and ytterbium (Yb) and erbium (Er) are doped by secondary hydrothermal. The surface temperature of the implants rises to a sufficiently high level due to the nano-shovel arrays upon irradiation with the 1,060 nm laser and Yb and Er enable up-conversion to generate ROS upon illumination with NIR-II light. Quercetin (Qr) is immobilized covalently on the surface of the TiO_2 nano-shovel with organosilane as the coupling reagent, while the positively charged LA adsorb electrostatically onto the negatively charged Qr. Qr as a flavonoid compound inhibits tumor growth while producing antibacterial, anti-inflammatory, and anti-osteoporotic effects [47,48]. LA can be catalyzed by ROS generated by the rare-earth doped TiO_2 nano-shovel during 1,060 nm laser irradiation to release NO. Hence, the system can quickly eliminate tumors and biofilms by the combined actions of PDT, PTT, Qr, and NO. At the same time, the nano-shovel structure and Qr promote osteogenic differentiation of bone marrow mesenchymal stem cells (BMSCs) and NO promotes angiogenesis and osseointegration (Scheme 1). The anti-tumor, anti-biofilm, and osseointegration properties are investigated systematically and verified *in vivo* and *in vitro*.

2. Material and methods

2.1. Preparation of TiO_2@UCN/Qr/LA

The medical-grade pure Ti substrate was cut into pieces with a size of 1 cm × 1 cm × 2 mm and cleaned with ethanol and deionized (DI) water for 20 min. The samples were immersed in 45 mL of TMAOH (1 mol/L), placed into a 50 mL autoclave, and subjected to a hydrothermal treatment at 200 °C for 12 h. After natural cooling, the samples were cleaned with deionized water (labeled as TiO_2). The samples underwent a second hydrothermal treatment in the autoclave in a solution containing 224.6 mg $Yb(NO_3)_3$ and 230.6 mg Er $(NO_3)_3$ at 240 °C for 30 h. Afterwards, the samples were cleaned with DI water and dried in an oven at 80 ℃ (labeled as TiO_2@UCN). To covalently modify with Qr, the samples were immersed in a 4% v/v 3-aminopropyltriethoxysilane (APTES) solution in absolute ethanol for 12 h for aminosilanization. The aminosilanized samples were soaked in the Qr solution (5×10^{-2} M and pH of 5) at 30 ℃ for 6 h (labeled as TiO_2@UCN/Qr). After cleaning with DI water, the samples were soaked in the LA solution (5×10^{-2} M) at 30 ℃ for 6 h (labeled as TiO_2@UCN/Qr/LA).

2.2. Characterization

The morphology, size and roughness of the nano-shovel were examined by field-emission scanning electron microscopy (FE-SEM, JSM-7001F, JEOL, Japan), transmission electron microscopy (TEM, Tecnai G20, FEI, USA) equipped with energy-dispersive spectroscopy (EDS), and atomic force microscopy (AFM, XE-100, Park Systems). The structure of the nano-shovel was analyzed by TEM and X-ray diffraction (XRD, Rigaku Dmax-3C, Cu Kα radiation) and X-ray photoelectron

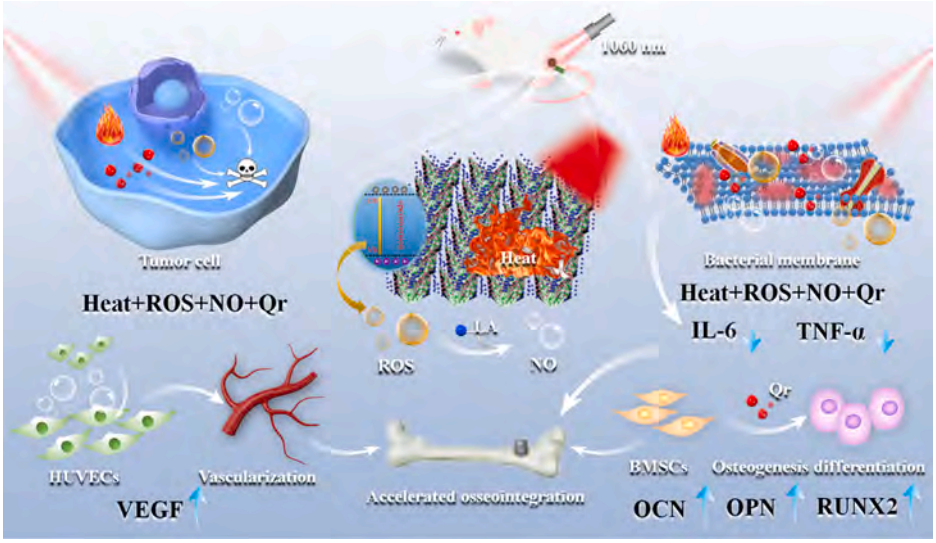

Scheme 1. Schematic illustration of TiO_2@UCN/Qr/LA nano-shovel on Ti implants for tumor ablation, biofilm elimination, vascularization and bone regeneration.

spectroscopy (XPS, K-Alpha, Thermo) was employed to determine the surface composition of the samples. The JS94 (Powereach, China) was used to determine the zeta potentials of the solutions and the JC2000D2 (Powereach, China) was employed to measure the contact angles and hydrophilicity of the samples. The electrochemical impedance spectroscopy (EIS) was tested by electrochemical workstation (CHI660E, Chenhua, China).

2.3. In vitro photothermal effects

The samples were put on a 24-well plate together with 1 mL of the phosphate buffer saline (PBS) and irradiated with the 1,060 nm laser with different power settign (0.3 W cm^{-2}, 0.6 W cm^{-2}, and 0.9 W cm^{-2}). A thermal imager was used to record the real-time temperature every minute for 15 min.

2.4. In vitro photocatalytic effects

The ROS (·OH and $^1O_2$) generated during 1,060 nm light irradiation were monitored with the aid of methyl violet (MV) and 1,3-diphenylisobenzofuran (DPBF), respectively. To reach the adsorption/desorption equilibrium, the samples were immersed in 1 mL of MV (0.025 g/L) and DPBF (0.07 g/L), respectively and placed in the dark for 10 min. After irradiation with the 1,060 nm laser with different power (0.3 W cm^{-2}, 0.6 W cm^{-2}, 0.9 W cm^{-2}), the optical densities (OD) of the residual MV and DPBF solutions were determined at 580 nm and 420 nm by ultraviolet–visible (UV–vis) spectrophotometry. The EMXPLUS10/12 (Bruker, Germany) was employed to monitor the electron spin resonance (ESR).

2.5. NO generation

The concentration of NO released from the samples upon irradiation with the 1,060 nm laser with different power (0.3 W cm^{-2}, 0.6 W cm^{-2}, 0.9 W cm^{-2}) was measured using a NO kit. The diazonium compounds formed were analyzed by UV–vis spectrophotometry at 540 nm.

2.6. In vitro antitumor ability

The osteosarcoma cells (Saos-2 cells, Shanghai Chinese Academy of Sciences) were cultured in the Dulbecco's modified eagle medium (DMEM) in an incubator (37 °C, 5% CO_2). The DMEM medium was supplemented with penicillin/streptomycin (1%) and fetal bovine serum (FBS 10%) and changed every day. To evaluate the anti-osteosarcoma performance, the UV-sterilized samples were put on a 24-well plate and 1 mL of Saos-2 cells (2×10^4 cells/cm^2) was added. Ten groups were studied (Table 1).

2.6.1. Live/Dead assay

The ablation effects of the osteosarcoma cells were evaluated with a live/dead kit. After the samples underwent different treatments (NIR-II - and NIR-II +) and washed with PBS, they were covered with 50 μL of the staining solution and incubated in the dark for 1 h. Four regions were chosen randomly for observation under a confocal scanning laser microscope (CLSM).

Table 1
Grouping and naming of samples.

Samples	Named	Samples	Named
Ti	Ti	Ti + NIR-II	Ti +
TiO_2	TiO_2	TiO_2 + NIR-II	TiO_2 +
TiO_2@UCN	TiO_2@UCN	TiO_2@UCN + NIR-II	TiO_2@UCN +
TiO_2@UCN/Qr	TiO_2@UCN/Qr	TiO_2@UCN/Qr + NIR-II	TiO_2@UCN/Qr +
TiO_2@UCN/Qr/LA	TiO_2@UCN/Qr/LA	TiO_2@UCN/Qr/LA + NIR-II	TiO_2@UCN/Qr/LA +

The groups indicated by "+" were irradiated with the 1,060 nm laser (0.9 W cm^{-2}) for 10 min and the temperature during irradiation was maintained at 48 ℃ using a water bath.

2.6.2. Annexin V/PI staining

The Saos-2 cells after different treatments (NIR-II - and NIR-II +) were digested with 2.5% trypsin (without EDTA) and collected by centrifugation. Annexin V-FITC and propidium iodide were added to the cells and incubated in the dark for 20 min and then the multicycle software was used to analyze the number of apoptotic cells.

2.6.3. Cell morphology

The morphology of the cells after different treatments (NIR-II - and NIR-II +) was examined by FE-SEM. After the cells were fixed with 3% glutaraldehyde for 1 h, dehydrated with gradient ethanol (20–100%) for 20 min, air-dried, and gold coated, they were observed by FE-SEM.

2.7. In vitro evaluation of the antibacterial activity

2.7.1. Antibiofilm assay

The bacteria used in the experiment were *Staphylococcus aureus* (*S. aureus*, ATCC 29213). The bacterial suspension (2 mL, 1×10^9 CFU/mL) was cultured with the samples at 37 °C to form biofilms after 2 days. The biofilm-covered samples were put in 1 mL of PBS and illuminated with a laser (1,060 nm, 0.6 W cm^{-2}) for 15 min to evaluate the antibiofilm capability. The temperature was maintained by placing the container with the samples in a constant temperature water bath.

The spread plate technique was adopted to assess the anti-biofilm forming capability. To dislodge the bacteria from samples, the samples after different treatments (NIR-II -, NIR-II + 25 °C and NIR-II + 45 °C) were sonicated in 1 mL of PBS. The standard agar medium was coated with 50 μL of the bacteria suspension diluted 1,000 times and incubated at 37 °C for 24 h. The agar plate with growing colonies was photographed and counted with Ti without irradiation being the control. The antibacterial ratio was calculated by the following formula:

$$\text{Antibacterial ratio} = \left[\left(\beta_{\text{control}} - \beta_{\text{sample}}\right) / \beta_{\text{control}}\right] \times 100\%$$

FE-SEM was performed to observe the morphology of the bacteria in the biofilms after fixing with 2.5% glutaraldehyde and rinsing with PBS. After serial dehydration with alcohol (20 to 100%) for 15 min and gold coating, they samples were examined by SEM. A CLSM was used to capture the 3D pictures of the biofilms stained with the live/dead kit (acridine orange/propidium iodide). After the irradiated samples were stained in the dark for 15 min, 4 regions were randomly selected and observed by CLSM.

2.7.2. Bacterial membrane permeability

O-nitrophenyl-*β*-D-galactopyranoside (ONPG) was used to investigate the membrane permeability of the biofilms. After different treatments (NIR-II -, NIR-II + 25 °C and NIR-II + 45 °C), the samples were treated with the ONPG solution (500 μL) and the OD value of the yellow supernatant was determined on a microplate reader at 420 nm.

2.7.3. Protein leakage

The samples were placed in the bacterial suspension (1 mL, 5×10^7 CFU/mL). After different treatments (NIR-II -, NIR-II + 25 °C and NIR-II + 45 °C), the bacterial suspension was centrifuged for 12 min at 5,000 rpm and 4 °C. An assay kit (P0010; Beyotime) was utilized to determine the quantity of leached proteins in the supernatant.

2.8. In vitro angiogenic activity of HUVECs

The human umbilical vein endothelium cells (HUVECs) were cultured the same way as the Saos-2 cells described in section 2.6, except that the power of the laser was 0.6 W cm^{-2} and the temperature was

45 °C.

2.8.1. Live/Dead assay

The experimental protocol was the same as that described in section 2.6.1.

2.8.2. VEGF secretion

The amount of VEGF secreted by the HUVECs was measured by the VEGF enzyme-linked immunosorbent assay (ELISA) kit (Abcam, UK). After different treatments (NIR-II - and NIR-II +), the HUVECs were cultured for 24 h before collecting the supernatant was collected and the VEGF released from the HUVECs was quantified according to the manufacturer's instructions.

2.8.3. Angiogenesis

ECMatrix™ (Millipore, Cat. No. ECM625) was used in the angiogenesis evaluation *in vitro*. Before the experiment, the ECMatrix™ gel was thawed at 4 °C overnight. After the viscous ECMatrix™ gel was mixed slowly mixed the diluted buffer, 50 μL of the solution were added to a pre-cooled 96-well plate and allowed to solidify for 45 min at 37 °C. After the different treatments (NIR-II - and NIR-II +), the HUVECs were cultured further for 3 days and the supernatant of the culture medium was collected. The HUVECs (2×10^4 cells) and collected medium were added to the solidified ECMatrix™ colloid and incubated for 4, 8, and 12 h at 37 °C. At each time point, photographs were taken from 4 random areas by a fluorescent inverted microscope.

2.9. In vitro osteogenic differentiation of BMSCs

The culturing conditions and treatments were the same as those for the HUVECs described in Section 2.8 except that the medium was change to the minimum essential medium alpha medium (α-Mem, Gibco, America).

2.9.1. Cell morphology

The morphology of the BMSCs on the samples after different treatments (NIR-II - and NIR-II +) was examined by the cytoskeleton assembly experiment. The cells were fixed with paraformaldehyde (4%) for 45 min and stained with FITC and DAPI for 1 h and 15 min in the dark, respectively. Four random areas were selected for CLSM.

2.9.2. Annexin V/PI staining

The experimental protocol was the same as shown in section 2.6.2.

2.9.3. Alkaline phosphatase (ALP) activity

After incubation for 4 and 7 days, the cells were lysed in the cell lysate and the intracellular ALP activity was determined quantitatively using the ALP detection kit.

2.9.4. Collagen secretion and matrix mineralization

Collagen secretion and matrix mineralization of the BMSCs cultured on the samples were analyzed quantitatively by Sirius Red (Sigma, America) and Alizarin Red (Aladdin, China) staining, respectively. After culturing for 7 and 14 days, the BMSCs were fixed with 4% paraformaldehyde and 75% ethanol and then stained with 0.1 wt% Sirius red and 40 mM alizarin red (pH = 4.2). The stain was cleaned with 0.1 M acetic acid and distilled water until it became colorless and then and eluted with 1 mL of 0.2 M NaOH/methanol (1:1) and 500 μL of 10% hexadecylpyridinium chloride. The OD values of these two solutions were measured at 570 nm.

2.9.5. Osteogenesis-related gene expression

The BMSCs were collected after culturing for 7 days and digested with trypsin (2.5%). The Eastep® super total RNA extraction kit (Promega) and PrimeScript™ RT reagent Kit (Takara) were employed to extract the cellular RNA and reverse transcribe the RNA, respectively. The StepOne real-time PCR system (Applied Biosystems) was used to determine the gene expression level (OCN, OPN, RUNX2). The primer sequences for the genes are listed Table S1 and the gene expression level of GADPH was used for normalization.

2.10. In vivo anti-tumor therapy

The animal experiments were approved by the Animal Ethics Committee of "Shanxi Medical University" and followed the stipulated regulations and 1% w/w sodium pentobarbital (30 mg/kg) was used in anesthesia. The tumor-bearing mouse model was established to evaluate the synergistic anti-tumor effects triggered by NIR-II *in vivo*. The Balb/c-nu mice (four-week-old) were assigned randomly to four groups (Ti, Ti +, TiO_2@UCN/Qr/LA, and TiO_2@UCN/Qr/LA +). After the hips of nude mice were injected with Saos-2 cells to form a mature tumor (diameter of 8 mm), the sample (Φ5 mm × 0.2 mm) was implanted in the tumor center. The light source for the irradiation group was a 1,060 nm laser (0.9 W cm^{-2}) and the first day of phototherapy was designated as day 0. Moreover, phototherapy was performed every other day for 10 min. The width and length of the tumor were recorded and the relative tumor size was V/V_0. The initial tumor - implant volume was recorded as V_0 and the tumor volume was calculated by the following formula:

$$V = (\text{tumor length}) \times (\text{tumor width})^2/2 - \text{implant volume}$$

On the 15th day, the tumor was taken out, photographed, weighed, and stained with hematoxylin and eosin (H&E), terminal deoxynucleotidyl transferase uridine triphosphate nick end labeling (TUNEL) and Ki-67.

2.11. In vivo antibacterial activity

An infection model was established in the tibia of Kunming mice (300 g) to evaluate the synergistic antibacterial effects triggered by the NIR-II laser *in vivo*. The mice were divided randomly into four groups (Ti, Ti +, TiO_2@UCN/Qr/LA, and TiO_2@UCN/Qr/LA +). The tibia of the anesthetized mice was implanted with a cylindrical sample (Φ1.5 mm × 3 mm) covered with the biofilm and the wound was sutured. One day after operation, the irradiation groups were irradiated with the 1,060 nm laser (0.6 W cm^{-2}) for 15 min and the temperature was recorded every minute. The mice were euthanized three days after surgery. The samples were taken out and the remaining bacteria on the surface were dislodged ultrasonically in 1 mL of PBS. The standard agar medium was coated with 50 μL of the bacteria suspension diluted 1,000 times to evaluate the bacteria resistance *in vivo*. Tissue infection around the implant was evaluated by H&E, Giemsa and CD31 staining and the levels of tumor necrosis factor-α (TNF-α) and interleukin 6 (IL-6) in the tissues were analyzed with the ELISA kit (Abcam) and immunofluorescence kit (Novus) in accordance with the manufacturers' instructions.

To verify that the penetration depth of the NIR-II laser was sufficient, the same method was adopted to assess the photothermal and antibacterial performance of the samples in New Zealand white rabbit (2 kg) femurs. The 808 nm (1 W cm^{-2}) and 1060 nm (1 W cm^{-2}) lasers were used as light sources.

2.12. In vivo osteogenic activity assay

The samples and surgical procedures were described in section 2.11 and the mice were euthanized after 4 weeks. The tibia of the mice with the samples were inspected by a micro-CT (VivoCT80, Scanco Medical, Switzerland) to establish a 3D model to quantify the amount of newly formed bone tissues. The tibia with the sample was fixed with paraformaldehyde (4%), dehydrated with gradient alcohol, impregnated with xylene, and embedded in polymethyl methacrylate to make the section which was stained with H&E and Safranin-O/Fast Green to evaluate osseointegration. Finally, the biological safety was investigated

by staining the main organs of the mice including the heart, liver, spleen, lung, and kidney with H&E.

2.13. Statistical analysis

All the experimental data were analyzed by the one-way analysis of variance and expressed as the mean ± SD with $n \geq 3$. The significance, high significance, and extreme significance were assessed by $^{*}p < 0.05$, $^{**}p < 0.01$, and $^{***}p < 0.001$, respectively.

3. Results and siscussion

3.1. Morphology of the nano-shovel

The preparation process is illustrated in Scheme 2. The uniform nanostructures mimicking crescent moon shovels are formed on the Ti plates after the alkali thermal reaction, and the coating thickness was about 650 nm (Figure S1). After doping with Yb and Er and immersion in the Qr and LA solutions, the morphology and roughness of the samples are basically unchanged (Figure S2, Fig. 1A and 1B). The TEM image (Fig. 1C) obtained from the scratched particles of TiO_2@UCN shows that doping with the rare-earth elements does not alter the (1 0 1) plane of TiO_2 with a lattice spacing of 0.35 nm. EDS confirms that Yb and Er are distributed uniformly on the TiO_2 nano-shovel. After sonication for 20 min or immersion in PBS at room temperature for 90 days, the nano-shovel is stable and adheres well to the substrate (Figure S3). The diffraction peaks of 54.1° and 70.2° in the XRD spectra further corroborate successful preparation of the TiO_2 nano-shovel with the anatase phase. TiO_2@UCN, TiO_2@UCN/Qr, and TiO_2@UCN/Qr/LA show similar XRD patterns as TiO_2, indicating that doping with rare-earth elements and grafting of activating factors do not alter the structure of TiO_2.

The surface chemical composition of TiO_2, TiO_2@UCN, TiO_2@UCN/Qr, and TiO_2@UCN/Qr/LA is determined by XPS as shown in Fig. 1E. Peaks of Ti 2p, O 1 s, and C 1 s are observed from the TiO_2 nano-shovel and Yb 4d and Er 4d peaks are observed from TiO_2@UCN confirming successful doping with Yb and Er. After silanization and covalent bonding of Qr on the surface of TiO_2@UCN, the intensity of the Yb 4d and Er 4d peaks decreases but the Si 2p peak appears from APTES (Figure S4) [49]. After introduction of LA, the N 1 s peak increases but the Si 2p peak decreases. In the high-resolution C 1 s spectrum of TiO_2@UCN/Qr (Fig. 1E1), peaks of C = C and C = O appear at 284.1 eV and 287.7 eV, respectively, indicating that Qr is modified on the silanized TiO_2@UCN surface [50]. The new peak of C = N (286.9 eV) observed from TiO_2@UCN/Qr/LA (Fig. 1E2) stems from the imine bond in LA corroborating grafting of LA [48]. The zeta potentials also verify grafting of LA on TiO_2@UCN/Qr (Fig. 1F). The potential of the negatively charged Qr solution decreases from 23.43 mV to −10.6 mV after mixing with the LA solution (−35.9 mV) suggesting LA is grafted onto TiO_2@UCN/Qr electrostatically [51].

The wettability is shown in Fig. 1G. The alkali reaction improves the hydrophilicity of Ti as shown by the decrease in the contact angle from 53.76° to 10.83° due to the morphological change. After doping with rare-earth elements, the contact angle on TiO_2@UCN increases to 33.63°. However, the contact angle on TiO_2@UCN/Qr decreases and further decreases to 10° after modification with LA. The improved hydrophilicity is expected to promote cell adhesion by increasing the affinity between the matrix and cell wall proteins [52].

The amount of Qr and LA are determined by ultraviolet spectrophotometry (Figure S6). The amounts of Qr immobilized on TiO_2@UCN/Qr and TiO_2@UCN/Qr/LA are 2.97 and 2.69 μg/cm^2 respectively, and the LA immobilized on TiO_2@UCN/Qr/LA is 1.25 μg/cm^2. Furthermore, the release curve of Qr in TiO_2@UCN/Qr/LA is measured and the results are shown in Figure S7. This result shows that the fixation of L-Arg can slow down the release of Qr. In the initial stage, the release of Qr is not in large amounts, but gradually reached a tipping point. Meanwhile, the First-order model and Higuchi model were established, and the first-order model have a higher degree of fit.

3.2. Photothermal and photocatalytic characteristics and controlled release of NO

The photothermal conversion ability is investigated by irradiating the samples in 1 mL of PBS with the 1,060 nm laser (0.6 W cm^{-2}). As shown in Fig. 2A and Figure S8, the change in the surface temperature of the samples with nano-shovels is basically the same with the temperature maintained at around 55 ℃ after irradiation for 8 min. In contrast, the highest temperature on Ti is only 45 ℃ thus verifying that the nano-shovel has good photothermal properties. The specific mechanisms of the photothermal response from TiO_2 nanostructures irradiated with NIR light have been elaborated in our previous study [53,54]. Firstly, the optical properties played a major role in the photothermal response, and the TiO_2 nanostructures have higher absorption and lower reflectivity than flat Ti [55]. Secondly, the nanostructures could improve the heat-transfer performance, thus facilitating photothermal conversion [56]. In addition, the doping of rare earth elements could significantly increase the absorption of TiO_2 in the near-infrared band, and the heat generated in photocatalysis might also contribute to the rising temperature [57]. The laser power affects the photothermal effects. As the power density of the 1,060 nm laser is increased from 0.3 W cm^{-2} to 0.9 W cm^{-2}, the temperature of TiO_2@UCN/Qr/LA increases rapidly from

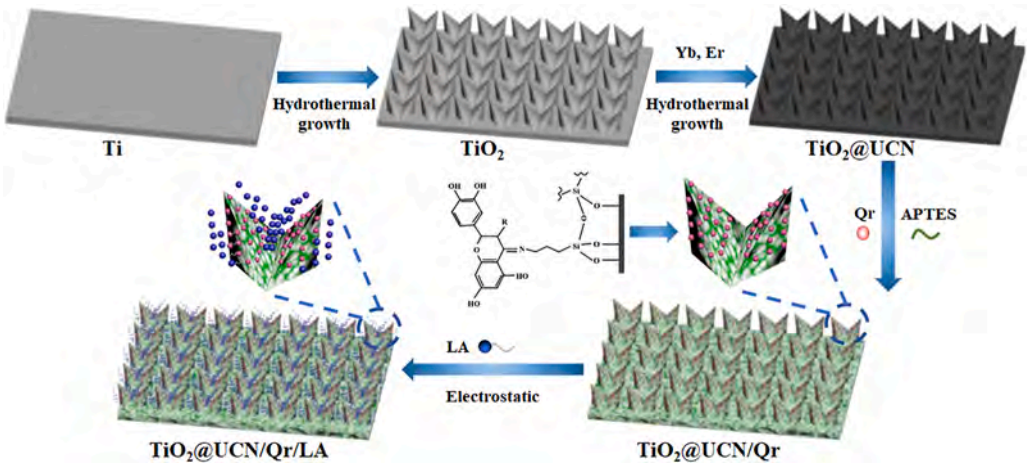

Scheme 2. Schematic illustration of the crafting process of TiO_2@UCN/Qr/LA nano-shovel on Ti implant.

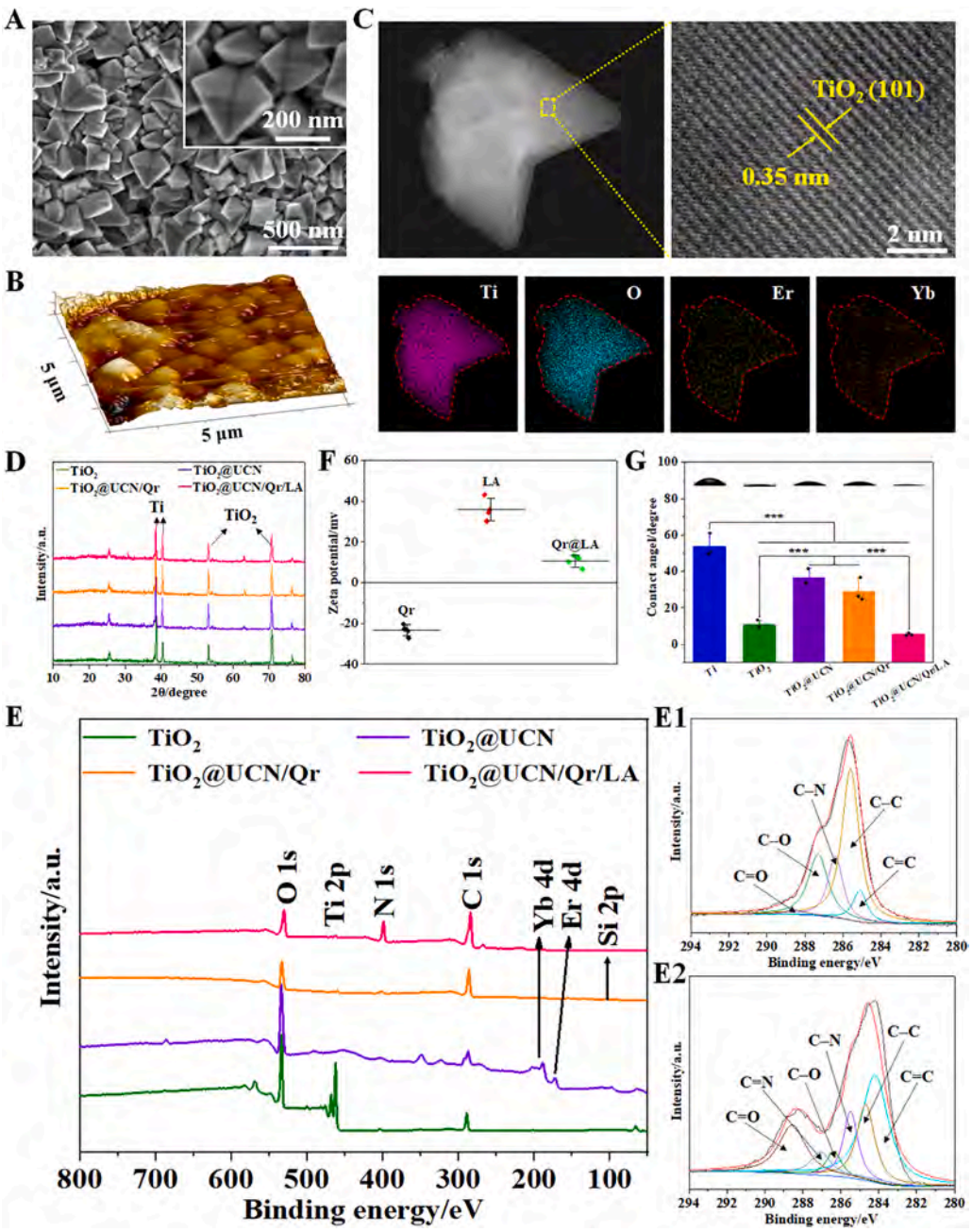

Fig. 1. (A) SEM image of TiO_2@UCN/Qr/LA; (B) AFM image of TiO_2@UCN/Qr/LA; (C) TEM image and elemental maps of the nano-shovel separated from TiO_2@UCN; (D) XRD patterns of TiO_2, TiO_2@UCN, TiO_2@UCN/Qr, and TiO_2@UCN/Qr/LA; (E) XPS survey spectra of TiO_2, TiO_2@UCN, TiO_2@UCN/Qr, and TiO_2@UCN/Qr/LA, (E1) C 1 s spectra of TiO_2@UCN/Qr and (E2) TiO_2@UCN/Qr/LA; (F) Zeta potentials on Qr, LA, and Qr@LA solution; (F) Contact angles on the samples (***$p < 0.001$).

42.4 °C to 63.4 °C (Fig. 2B). The heating and cooling curve illustrates the high efficiency and stability of TiO_2@UCN/Qr/LA in the photothermal conversion process (Fig. 2C) consequently providing the foundation for photothermal therapy.

The amounts of $^1O_2$ and ·OH produced by irradiation are determined by DPBF and MV, respectively. Figure S9 shows the change in the absorption peak intensity at 420 nm for the different samples after irradiation with the 1,060 nm laser for 15 min (0.9 W cm^{-2}). Compared to the blank control, the absorption peaks of Ti and TiO_2 only exhibit small decline, but those of TiO_2@UCN, TiO_2@UCN/Qr, and TiO_2@UCN/Qr/LA decrease significantly to the same level, implying that a lot of $^1O_2$ is generated and modification with Qr and LA has no obvious effects on the production of $^1O_2$. On the other hand, the yield of $^1O_2$ increases with illumination time and laser power. The results of ·OH produced upon irradiation are similar to those of $^1O_2$. It has been shown that optical absorption, electron-hole pair separation, and crystallinity of TiO_2 can be enhanced by doping with rare-earth elements, nonmetals, and transition metals [58]. The doping ions can reduce the band gap and expand the light response range. There existed some intermediate energy levels in the band gap of TiO_2@UCN owing to the introduction of the dopants [59,60]. Another reason might be that the doped ions could introduce the oxygen vacancie to prevent electron-hole pairs recombination or cause charge imbalance which could adsorb more hydroxide ions or O_2 to form hydroxyl radicals, thus jointly improving the photocatalytic activity under near-infrared light [61,62]. As shown in Fig. 2D, the diameter of the loop for TiO_2@UCN decreases significantly, suggesting reduced resistance of charge transport and better charge transfer after doping of Yb and Er. The decrease in the semicircle at intermediate frequencies indicates that the smaller interfacial resistance of TiO_2@UCN promotes transfer and transportation of charges leading to improved photocatalytic properties [63]. The amount of ROS generated by Ti and TiO_2@UCN/Qr/LA under 1,060 nm laser irradiation is determined by ESR (Fig. 2E and F). A negligible ESR signal is detected from Ti but that from TiO_2@UCN/Qr/LA is strong, indicating that TiO_2

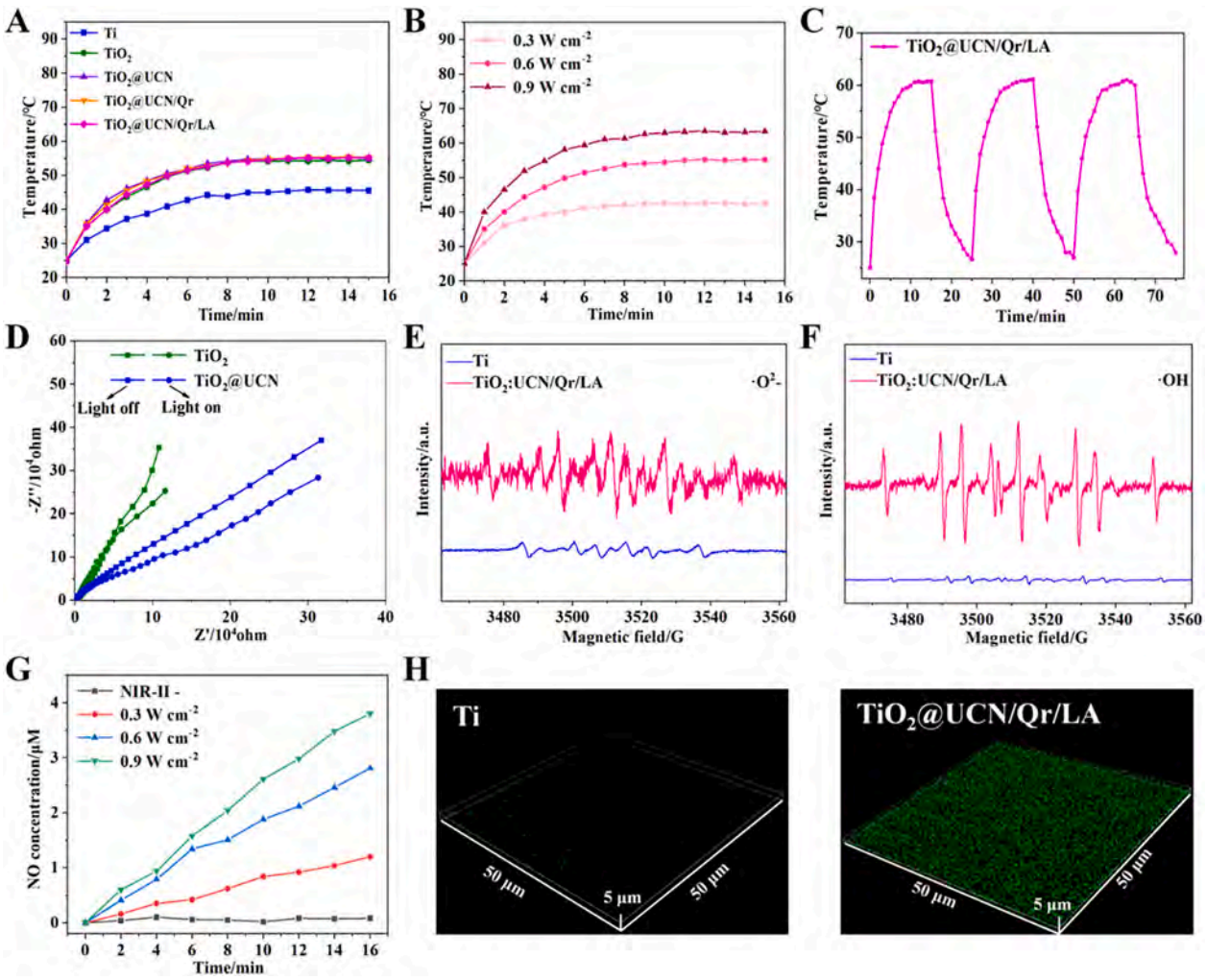

Fig. 2. Evaluation of heat, ROS, and NO: (A) Photothermal curves of Ti, TiO_2, TiO_2@UCN, TiO_2@UCN/Qr, and TiO_2@UCN/Qr/LA upon 1,060 nm light irradiation (0.6 W cm^{-2}); (B) Temperature change of TiO_2@UCN/Qr/LA during 1,060 nm light irradiation (0.3 W cm^{-2} – 0.9 W cm^{-2}); (C) Heating and cooling curve of TiO_2@UCN/Qr/LA for 3 cycles; (D) EIS of TiO_2 and TiO_2@UCN with or without irradiation; (E) $^1O_2$ and (F) ·OH detected from Ti and TiO_2@UCN/Qr/LA by ESR with the DMPO probe; (G) NO release from TiO_2@UCN/Qr/LA upon 1,060 nm light irradiation (0.3 W cm^{-2} – 0.9 W cm^{-2}); (H) Fluorescence images of NO of Ti and TiO_2@UCN/Qr/LA after 1,060 nm laser irradiation.

nano-shovel doped with Yb and Er produces $^1O_2$ and ·OH during NIR-II light exposure due to the up-conversion property and therefore, the photocatalytic properties are improved significantly.

The conversion of LA to NO in the catalytic reactions has been explored in the field of biomedicine [45] and the NIR-responsive TiO_2@UCN/Qr/LA provides the suitable platform to realize PTT, PDT, and ROS-responsive NO therapy at the same time. Release of NO from TiO_2@UCN/Qr/LA during 1,060 nm laser irradiation is presented in Fig. 2G. TiO_2@UCN/Qr/LA cannot produce NO without laser irradiation and release of NO triggered by ROS exhibits a positive correlation with the laser power. When it is increased from 0.3 W cm^{-2} to 0.9 W cm^{-2}, the amount of NO changes 1.2 μM to 3.8 μM. The DAF-FM probe further verifies generation of NO rendered by catalysis of ROS. After 1,060 nm laser irradiation, TiO_2@UCN/Qr/LA shows obvious NO fluorescence staining compared to Ti (Fig. 2H). In addition, the N 1 s high-resolution spectra of TiO_2@UCN/Qr/LA irradiated with or without 1060 nm laser were analyzed by XPS (Figure S10). As shown in Fig. 1, after TiO_2@UCN/Qr/LA was irradiated with 1060 nm laser, the proportion of C = O bond reduced, indicating the formation of NO and citrulline.

3.3. *In vitro* therapeutic effects on osteosarcoma

The killing effects of Saos-2 cells is investigated *in vitro*. As shown in Fig. 3A, the live/dead staining assay reveals that most of the cells exhibit green fluorescence without laser irradiation. The sporadic dead cells on TiO_2@UCN/Qr and TiO_2@UCN/Qr/LA can be attributed to the anti-tumor effects of Qr [47,48]. After laser irradiation for 10 min, most of cells in the Ti + and TiO_2 + groups survive, even though the temperature rises to 48 ℃. After doping with the rare-earth elements, a few dead cells appear from the TiO_2@UCN + group showing that PDT enhances low-temperature PTT in killing tumor cells. Introduction of Qr further increases the number of dead cells in the TiO_2@UCN/Qr + group. Surprisingly, almost all the tumor cells in the TiO_2@UCN/Qr/LA + group are dead indicative of the synergistic anti-tumor effects of hyperthermia, ROS, Qr, and NO. Flow cytometry is performed and as shown in the Fig. 3B, the Saos-2 cells show great activity without light irradiation but in contrast, those in the TiO_2@UCN/Qr/LA + group undergo apoptosis (64.7%) according to live/dead staining.

The morphological changes of the tumor cells are monitored by SEM (Fig. 3C). The Saos-2 cells of the Ti, TiO_2@UCN, and TiO_2@UCN/Qr/LA groups spread well. After 1,060 nm laser illumination 10 min, the cell morphology of the Ti + group does not change but those of the TiO_2@UCN + and TiO_2@UCN/Qr/LA + groups begin to shrink, especially the TiO_2@UCN/Qr/LA + group. The therapeutic effects of normal cells are investigated under the same conditions. As shown in Figure S11, although some of the normal cells die, they do not ablate as

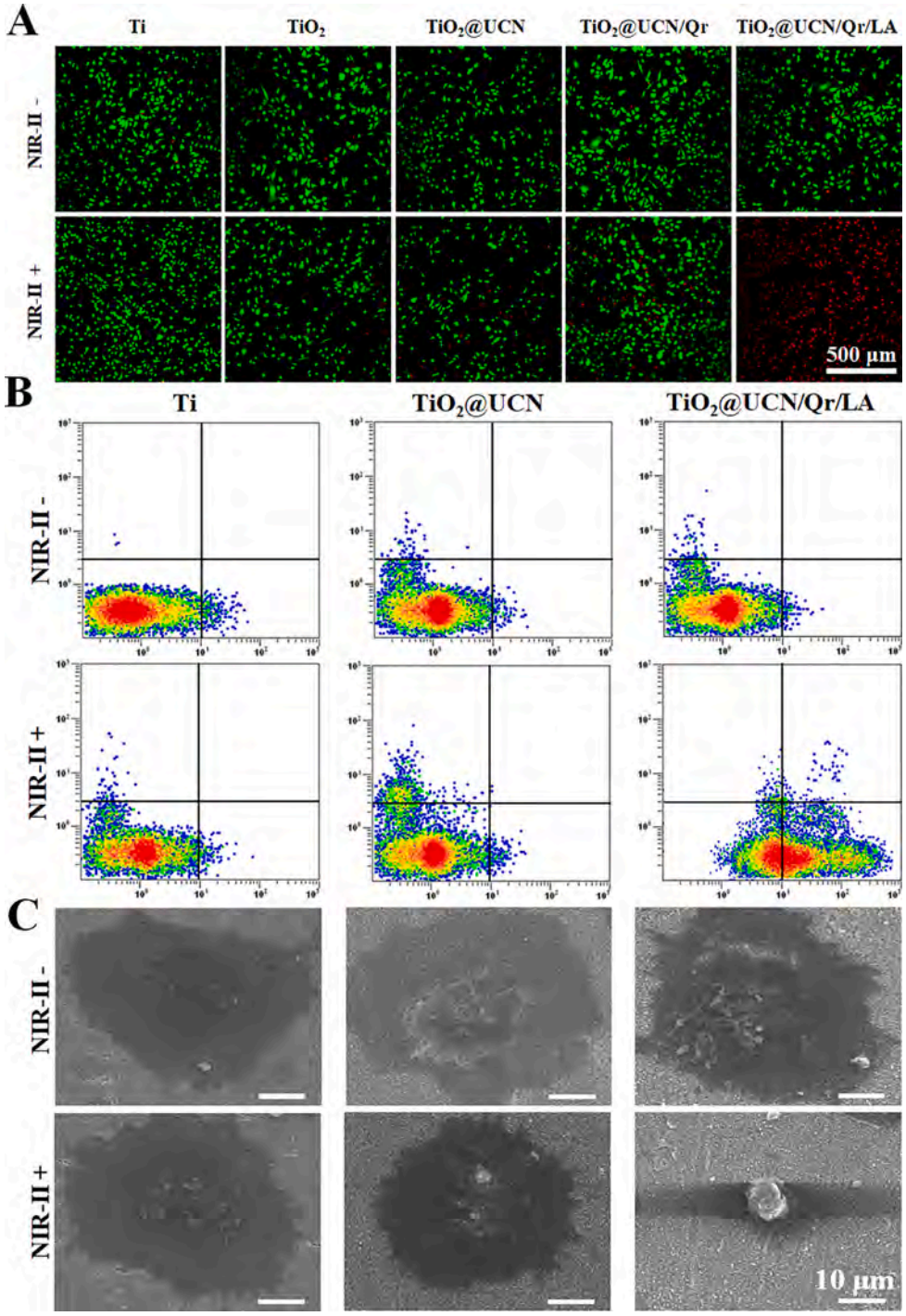

Fig. 3. *In vitro* osteosarcoma cell ablation of Ti, TiO_2, TiO_2@UCN, TiO_2@UCN/Qr, and TiO_2@UCN/Qr/LA: (A) CLSM images of Saos-2 cells (green/red represents live/dead cells); (B) Flow cytometry results of Saos-2 cells; (C) SEM images of Saos-2 cells.

extensively as the Saos-2 cells. The main reason is that tumor cells are more sensitive to heat than normal cells [60] and therefore, the photo-therapeutic effects of TiO_2@UCN/Qr/LA are quite good giving rise to tumor cell apoptosis and tumor ablation as a result of synergistic PTT, PDT, Qr, and NO effects. Previous studies have pointed out that Qr had an inhibitory effect on multiple cancer cells and can inhibit a variety of enzymes in cancer cells to participate in cell proliferation and signal transduction pathways [61,62]. Meanwhile, Qr also played an anti-tumor role by inducing apoptosis of tumor cells [63,64]. Moreover, the synergistic effect of Qr and chemotherapy drugs or radiotherapy could effectively kill tumors, and Qr could also protect normal cells from the side effects of chemotherapy and radiotherapy [65,66].

3.4. *In vitro* bacterial biofilm elimination

The anti-biofilm efficiency is assessed by the spread plate method (Fig. 4A) and the antibacterial rate is calculated by counting the number of colony forming units (Fig. 4B). All the samples do not exhibit apparent bacteriostasis against biofilms without NIR-II light irradiation (Figure S12). After irradiation with the 1,060 nm laser for 15 min at 25 ℃, the Ti + and TiO_2 + groups still show negligible bactericidal effects, but the antibacterial efficiency of the TiO_2@UCN +, TiO_2@UCN/Qr +,

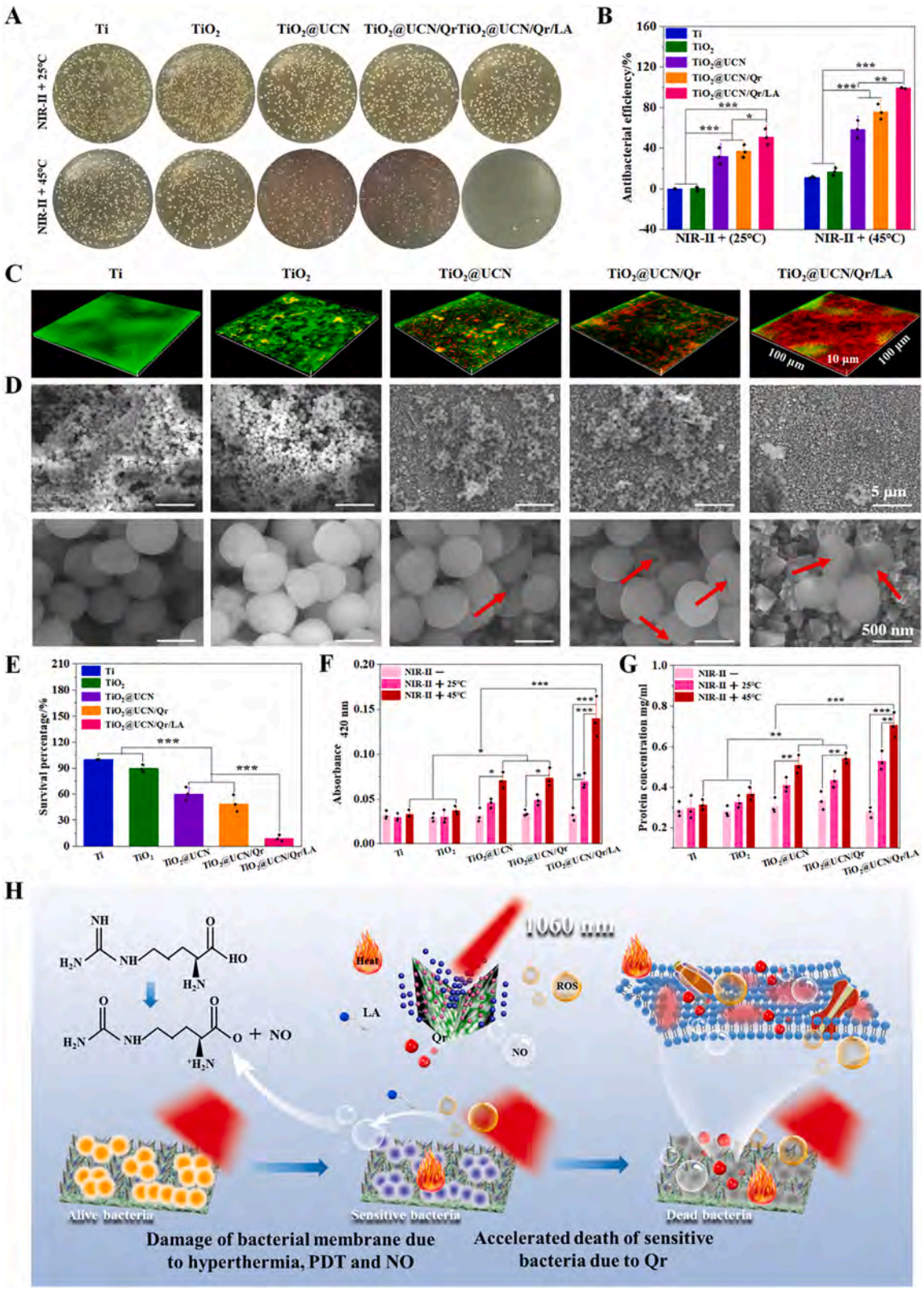

Fig. 4. Anti-biofilm efficiency of Ti, TiO_2, TiO_2@UCN, TiO_2@UCN/Qr, and TiO_2@UCN/Qr/LA *in vitro* and corresponding mechanism: (A) Photographs of bacteria colonies detached from the *S. aureus* biofilms after different treatments; (B) Anti-biofilm efficiency based on the spread plate results; (C) Fluorescence images, (D) SEM images, and (E) Biofilm survival percentages of *S. aureus*; (F) Bacterial membrane permeability after different treatments; (G) Protein leakage of *S. aureus* after different treatments; (H) Biofilm elimination mechanism of TiO_2@UCN/Qr/LA nano-shovel; (*$p < 0.05$, **$p < 0.01$, ***$p < 0.001$).

and TiO_2@UCN/Qr/LA + groups is 32.2%, 37%, and 51.1%, respectively. The results show that the ROS produced by TiO_2@UCN has some bactericidal ability and introduction of Qr and NO produces further improvement. However, the activity is not sufficient to eliminate biofilm formation completely without PPT. When the temperature rises to 45 ℃, the antibacterial efficiency of the TiO_2@UCN + and TiO_2@UCN/Qr + groups increases to 58.8% and 75.7%, respectively, indicating that the combination of hyperthermia, ROS, and Qr produces weak bactericidal effects without NO. In contrast, the antibacterial efficiency of the TiO_2@UCN/Qr/LA + at 45 ℃ reaches 99.3% revealing that a combination of low-temperature PTT, PDT, Qr, and NO is essential to eliminate biofilms.

The anti-biofilm effects are evaluated quantitatively by live/dead staining and the 3D fluorescence images after exposure to the 1060 nm laser for 15 min are depicted in Fig. 4C. The biofilm of the Ti + group is stained green indicating that the bacteria survive despite laser irradiation. The green area of the TiO_2 + group decreases slight mainly because of PTT and there is some biofilm inhibition. Some red fluorescence appears from the TiO_2@UCN + group indicating that ROS generated enhance the antibacterial activity. After introduction of Qr, the red area increases but biofilms are not eliminated completely. After LA is immobilized on the surface of TiO_2@UCN/Qr and NO is added to kill bacteria, the TiO_2@UCN/Qr/LA + group exhibits excellent anti-biofilm effects.

The morphology of the *S. aureus* biofilms is observed by SEM (Fig. 4D). After exposure to the 1,060 nm laser for 15 min, the biofilms of the Ti + and TiO_2 + groups are dense and the bacteria have the typical spherical morphology with the complete membrane structure. In comparison, the biofilms of the TiO_2@UCN + and TiO_2@UCN/Qr + groups are largely eliminated and the bacteria survival percentage drops to 60.3% and 49% (Fig. 4E), respectively. Furthermore, atrophy and deformation can be observed from some bacteria. Only a trace amount of bacteria remains in the TiO_2@UCN/Qr/LA + group but they are severely shriveled and distorted.

The degree of bacterial membrane damage is measured by ONPG which can penetrate damaged cell membranes and react with bacterial intracellular β-d-galactosidase to form o-nitrophenol [67]. After incubation for 15 min in the dark, hydrolysis of ONPG shows insignificant changes (Fig. 4F), indicating negligible impact on bacteria without light irradiation. Comparatively, even when the temperate is 25 ℃, the TiO_2@UCN + and TiO_2@UCN/Qr + groups show extensive hydrolysis of ONPG compared to the Ti + and TiO_2 + groups. The permeability of the bacterial membrane of the TiO_2@UCN/Qr/LA + group increases, implying that ROS damage the bacterial cell membrane. When the temperate is increased to 45 °C, hydrolysis of ONPG of the TiO_2@UCN +, TiO_2@UCN/Qr +, and TiO_2@UCN/Qr/LA + groups increases further. In particular, the combination of the PTT, PDT, and NO improves the bacterial membrane permeability of the TiO_2@UCN/Qr/LA group. Meanwhile, membrane destruction results in leakage of cytoplasm [68-70] which shows a similar trend as hydrolysis of ONPG (Fig. 4G).

Generally, once bacteria were adsorbed on the inert surface, a large number of polysaccharides, lipids and other polymers would be produced to wrap around the bacteria, thus forming a natural barrier layer. The protective layer could prevent antibiotics from embedded in the bacterial outer wall and increase the difficulty of removing biofilm [71,72]. Previous studies have confirmed that ROS could destroy the extracellular matrix by degrading biofilm components, leading to the elimination of biofilms [73]. For instance, ROS could react with the ribonucleic acid, leading to the destruction of the DNA bonds and collapse of the extracellular DNA structural framework [74]. However, a large amount of ROS was required to effectively eliminate biofilm due to the antioxidant system of biofilm. NO molecules, as a free radical, can not only weakened the protection of biofilms by the antioxidant system, but also greatly enhance the ability of ROS to penetrate into biofilms [74]. Meanwhile, NO also could react with ROS to produce more deadly peroxynitrite (ONOO–) molecules (Figure S13) which can destroy bacterial cell membranes effectively [75,76]. In addition, some studies have shown that Qr could increase the permeability of the cell membrane by destroying the integrity of the bacterial cell membrane [77,78]. At the same time, the protein synthesis in the bacteria could be blocked, thereby affecting the physiological functions of the protein in the bacteria [79].

According to the antibacterial results, Fig. 4H shows the mechanism associated with biofilm elimination. Hyperthermia and ROS generated by the up-converted TiO_2@UCN/Qr/LA during NIR-II light exposure cause initial oxidation damage to the bacterial membrane. NO produced by LA by ROS catalysis further cripples the antioxidant defense system of the bacteria and destroys the integrity of the cell membrane. Posteriorly, the released Qr acts as a bactericide to destroy the bacteria and the irreversible damage to the cell membrane exacerbates loss of intracellular components leading to death. Our results reveal the combined effects of PTT, PDT, Qr and NO produced by TiO_2@UCN/Qr/LA under NIR-II light irradiation are responsible for the excellent outcome.

3.5. *In vitro angiogenesis*

The prerequisite to osseointegration at the bone-implant interface is angiogenesis [80] and the angiogenic activity is investigated by culturing HUVECs on the samples. As shown in Fig. 5A, all the samples show no obvious cytotoxicity with or without irradiation. In particular, the TiO_2@UCN/Qr/LA + group promotes HUVECs proliferation attributed to NO. VEGF secretion is an indicator of the HUVECs activity and key factor in angiogenesis [81] and the level of VEGF secreted by HUVECs is quantified by ELISA (Fig. 5B). Similar to fluorescent staining, only the HUVECs of the TiO_2@UCN/Qr/LA + group shows more VEGF secretion. The angiogenesis ability of HUVECs is evaluated by an angiogenesis kit containing ECMatrix™ gel. During cultivation, the HUVECs begin to self-assemble after 4 h forming branched nodes and meshed circles (Fig. 5C). The branching and reticular circles are enlarged after 8 h and parallel tubular cell lines are seen after 12 h. The number of points and circles as well as tube formations of the TiO_2@UCN/Qr/LA + group increase significantly compared to the other groups at the same time point. Previous studies showed that NO diffusion in vasculature contributed to vascular permeability, and longer-term responses such as HUVECs survival, migration and proliferation [82]. Meanwhile, NO could up-regulate the expression of VEGF, thereby promoting angiogenesis [82]. On the other hand, LA catalyzed by ROS could produce L-citrulline with excellent biocompatibility, which might also affect the physiological function of cells [83]. At the same time, the abundant vascular network provides the necessary nutrients and oxygen for osteoblasts and osteoinductive growth factors giving rise to enhanced osseointegration [84,85].

3.6. *In vitro response of BMSCs*

The biological interface requires the proper cytocompatibility and osteogenic activity for osseointegration. As precursors of osteoblasts, BMSCs play a crucial role in bone regeneration [86]. The morphology, proliferation, apoptosis, osteogenic differentiation, and expression levels of related genes of BMSCs are therefore monitored to evaluate the osteogenic ability. As shown in Fig. 6A and S14, the F-actin and cell nuclei are stained with FITC and DAPI to observe the cell morphology, adhesion and spread activity. With or without light exposure, the BMSCs on all the samples exhibit the same trend, indicating that the effects of light on the BMSCs at 45 °C are minimal. Compared with Ti and TiO_2, the BMSCs spread poorly on TiO_2@UCN and the number also decreases possibly because of the poor hydrophilicity of TiO_2@UCN after doping with rare earth elements. However, most of the BMSCs show the typical slender shape with numerous filamentous feet on TiO_2@UCN/Qr and TiO_2@UCN/Qr/LA, suggesting that Qr benefits growth and proliferation of BMSCs. There is no obvious difference between the TiO_2@UCN/Qr

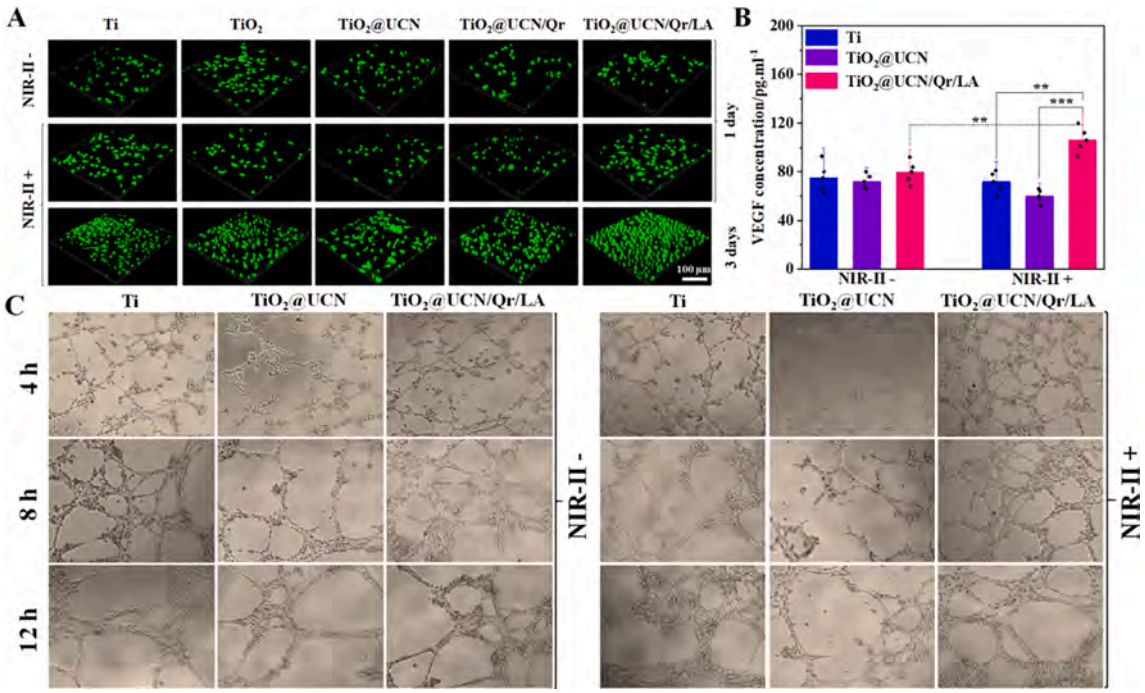

Fig. 5. *In vitro* angiogenesis evaluation of Ti, TiO_2, TiO_2@UCN, TiO_2@UCN/Qr, and TiO_2@UCN/Qr/LA: (A) Fluorescence images of HUVECs (green/red representing live/dead cells); (B) VEGF concentrations secreted by HUVECs; (C) Angiogenesis ability of HUVECs (**p < 0.01, ***p < 0.001).

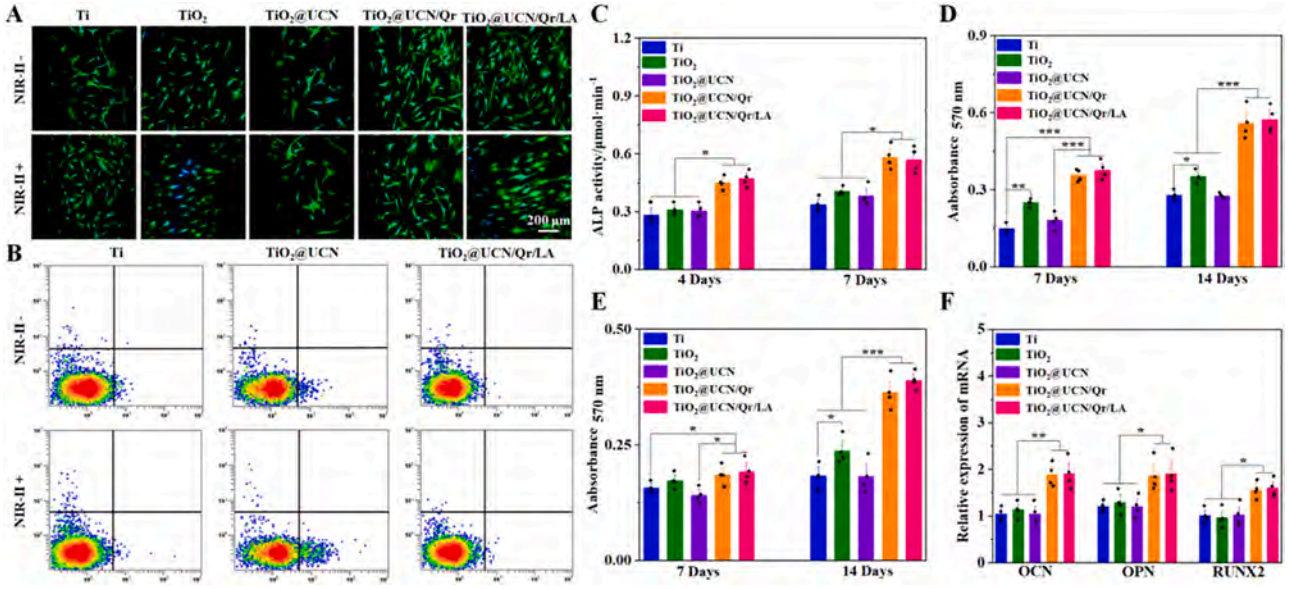

Fig. 6. Response of BMSCs *in vitro*: (A) Fluorescence images of BMSCs after culturing for 1 day; (B) Flow cytometry results of BMSCs; (C) ALP activity, (D) Collagen secretion, and (E) ECM mineralization after culturing 7 and 14 days; (F) Osteogenisis-related gene (OCN, OPN and RUNX2) expressions after culturing for 5 days (*p < 0.05, **p < 0.01, ***p < 0.001).

and TiO_2@UCN/Qr/LA groups with respect to cell viability and morphology, indicating that LA does not affect the BMSCs.

Flow cytometry (Fig. 6B) shows early apoptotic cells in the TiO_2@UCN group and after irradiation with the 1,060 nm laser, the number of the early apoptotic cells increases significantly, indicating that both doping with rare-earth elements and generation of ROS by TiO_2@UCN under light irradiation have adverse effects on BMSCs. However, with or without light irradiation, the cells on TiO_2@UCN/Qr/LA regain their vitality.

ALP is a key indicator of early differentiation of osteogenesis and so up-regulation of ALP is meaningful for osteogenesis [54]. Quantitative analysis of ALP is shown in Fig. 6C. The BMSCs cultured on TiO_2 and TiO_2@UCN for 3 and 7 days show stronger ALP activity than Ti, suggesting that TiO_2 NSs promote early proliferation of BMSCs. Moreover, Qr promotes osteogenic differentiation [47,48]. Osteogenic differentiation of BMSCs in the late stage is evaluated by quantitative determination of collagen secretion and ECM mineralization (Fig. 6D and E). With the exception of TiO_2@UCN, the results are in line with the ALP activity. The level of collagen and mineralization on the surface of the Qr-functionalized nano-shovel is significantly higher than that of other groups after 7 days and it is more apparent after 14 days. The results demonstrate that surface functionalization with Qr mitigates the adverse

effects of rare-earth doping and the nano-shovel structure plays a key role in accelerating osteogenic differentiation.

The expression of osteogenic related genes (OCN, OPN and RUNX2) is analyzed by RT-QPCR. After incubation in the osteogenic induction medium for 5 days, the expression level of the osteogenic genes on the Qr-modified surface is significantly higher than that of the other samples (Fig. 6F). The results confirm that immobilization of Qr on the surface improves the osteogenic activity.

It had been reported the cell behavior was sensitive to the nanoscale topography of the substrate, and the proper size and morphology of the TiO_2 nano-shovel was conducive to cell growth [87]. The nanopatterned surface had been shown to promote the expression of integrins and formation of focal adhesions, consequently promoting assembly of the cytoskeletal structure [88,89]. Meanwhile, similar to the adhesion properties of marine organisms (such as mussel adhesion protein), the catechol functionality of Qr on the implant might be outer-oriented and exposed to the cells, thus favoring cell adhesion/proliferation and increasing the metabolic activity [90].

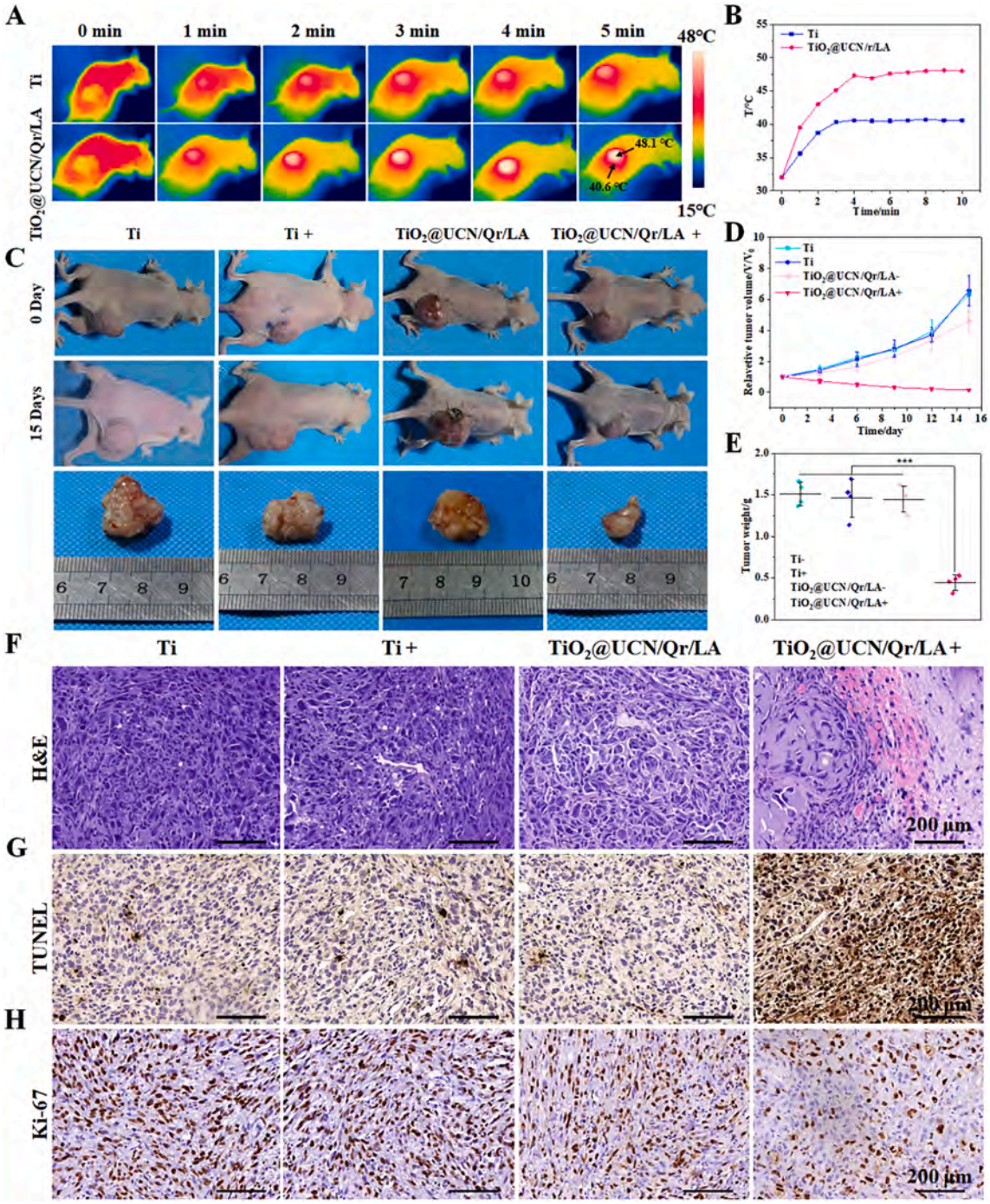

Fig. 7. *In vivo* treatment of osteosarcoma: (A) Infrared images and (B) Heating curves of the Ti and TiO_2@UCN/Qr/LA groups at the tumor sites of Saos-2 tumor-bearing mice irradiated with the 1,060 nm laser (0.9 W cm^{-2}); (C) Photographs of tumors on day 0 and day 15 of the Ti, Ti +, TiO_2@UCN/Qr/LA, and TiO_2@UCN/Qr/LA + groups; (D) Relative tumor volume changes with time; (E) Tumor weights on day 15; (F) H&E, (G) TUNEL and (H) Ki-67 staining of tumor sites on day 15 (***$p < 0.001$).

3.7. In vivo tumor ablation

In view of the favorable therapeutic effects of TiO_2@UCN/Qr/LA *in vitro*, the xenograft model of nude mice is established to evaluate the effects *in vivo*. As shown in Fig. 7A and B, the photothermal effects are recorded. The temperature of the osteosarcoma tissue rises to 48 °C within 4 min when the TiO_2@UCN/Qr/LA tumor is irradiated with the 1,060 laser but pure Ti only reaches a temperature of 40.6 °C. At the same time, the temperature of the surrounding tissues is lower than that of the osteosarcoma tissue boding well for less damage. The tumor volume changes of the Ti and TiO_2@UCN/Qr/LA groups with or without light irradiation on day 0 and day 15 are displayed in Fig. 7C. It is evident that the tumors of the Ti, Ti +, and TiO_2@UCN/Qr/LA groups increase after 15 days but in contrast, that of the TiO_2@UCN/Qr/LA + group decreases significantly in volume.

To further quantify the effect of anti-osteosarcoma, the relative tumor volume (V/V_0) is calculated and the tumor is weighed (Fig. 7D and 7E). After light-triggered therapy, the relative volume of the tumor of the TiO_2@UCN/Qr/LA + group decreases to 0.156 and the weight is 0.447 g showing excellent anti-tumor activity. The trend of the tumors of the Ti and Ti + groups is basically the same with the relative tumor volume increasing to 6 and weight increasing to about 1.5 g, indicating that laser irradiation alone cannot eradicate the tumor. The TiO_2@UCN/Qr/LA group also shows the weak anti-osteosarcoma ability on account of the inhibitory effects of Qr on cancer cells [48]. H&E (Fig. 7F) and TUNEL staining (Fig. 7G) reveals extensive necrosis of osteosarcoma cells in the TiO_2@UCN/Qr/LA + group, while there is a mass of osteosarcoma cells in the other groups. Meanwhile, the tumor slices are stained with Ki-67 antibody to investigate the cellular proliferation activity of tumors from different groups. The TiO_2@UCN/Qr/LA + group causes negligible cellular proliferation, whereas evident tumor cell proliferation is observed from the Ki-67 staining images in the treatment groups of Ti, Ti +, and TiO_2@UCN/Qr/LA groups, confirming the prominent *in vivo* therapeutic efficacy (Fig. 7H). In summary, the combined actions of hyperthermia, ROS, and NO produces the desirable effects observed from the TiO_2@UCN/Qr/LA group, and the treated nude mice survived longer (Figure S15).

3.8. In vivo anti-infection analysis

To evaluate the anti-biofilm ability of TiO_2@UCN/Qr/LA *in vivo*, the Ti and TiO_2@UCN/Qr/LA samples with intact *S. aureus* biofilms are implanted into the tibia of mice. In the light-exposed group, the implant sites are irradiated with the 1,060 nm laser and the photothermal conversion ability is evaluated *in vivo* with the aid of a thermal camera to record the temperature in real time (Fig. 8B). The temperature of the TiO_2@UCN/Qr/LA group increases rapidly from 27 °C to 44.1 °C within 4 min and then stabilizes, whereas that of the Ti group only rises to 38.2 °C (Fig. 8C). After two days, the samples are taken out and sonicated. The bacterial solution is cultured in the medium at 37 °C for 12 h and spread on the plate. As shown in Fig. 8D and Figure S16, the Ti and Ti + groups do not exhibit any antibacterial activity and the TiO_2@UCN/Qr/LA group show almost no bactericidal effects. However, the antibacterial rate of TiO_2@UCN/Qr/LA + reaches 98.7%.

To prove that the NIR-II light has stronger tissue penetrating ability than NIR-I light, the photothermal and anti-biofilm capabilities of TiO_2@UCN/Qr/LA in rabbit femurs are assessed upon irradiation with the 1,060 nm and 808 nm lasers (1 W cm^{-2}), respectively. As shown in Figure S17, the heating rate is higher under the 1,060 nm laser irradiation at the same time point before stabilizing at 45.8 °C, which is 8 °C higher than that for the 808 nm laser. Furthermore, TiO_2@UCN/Qr/LA under 1060 nm laser irradiation shows better anti-biofilm ability in the rabbit femur. These results show that the biofilm of the TiO_2@UCN/Qr/LA group can be removed *in vivo* by NIR-II laser irradiation.

During the perioperative period, the tissues surrounding the implants are susceptible to exogenous infection and after infection, inflammatory cells respond quickly and migrate to the infected site. Severe inflammation may also lead to implantation failure [91-93] and therefore, inflammation and bacterial infection of the soft tissues around the implants after phototherapy are evaluated by H&E staining and Giemsa staining, respectively (Fig. 8E). As expected, significant acute inflammation and neutrophil infiltration (indicated by black arrows) are observed by H&E staining from the Ti and Ti + and TiO_2@UCN/Qr/LA groups. At the same time, many adherent bacteria appear from the tissues (indicated by yellow arrows) in these groups after Giemsa staining. On the contrary, only a litter neutrophils and bacteria are found from the TiO_2@UCN/Qr/LA + group, indicating excellent antibacterial activity *in vivo* after light irradiation.

The immune response is also evaluated by ELISA and immunofluorescence. As shown in Fig. 8F, G, and H, the levels of pro-inflammatory cytokines (IL-6 and TNF-α) in the TiO_2@UCN/Qr/LA + group are lower than those of the other three groups. Immunity plays a key role in osseointegration and the anti-inflammatory effects of implant affect subsequent angiogenesis and new bone formation [94]. Hence, the material-mediated immune response of the samples without biofilms is evaluated (Figures S18). Compared to the blank control, although the samples without biofilms still show inflammatory response, it is far lower than those with biofilms, suggesting that bacterial infection is the main cause of inflammation. The TiO_2@UCN/Qr/LA group without biofilms shows the lowest inflammatory response because Qr alleviates inflammation [47,48].

In addition, *in vivo* angiogenesis was observed by CD31 immunohistochemistry and the results are shown in Fig. 8I. As expected, the TiO_2@UCN/Qr/LA + group has the best angiogenesis effect *in vivo*.

3.9. In vivo bone formation

Osseointegration of implants is inhibited by infection and therefore, new bone formation on the biofilm-covered implants is studied. The newly formed bone around the implants four weeks after implantation is investigated by micro-CT and histological staining. The reconstructed 3D images are shown in Fig. 9A (new bone shown in grey and implant in pink). The new bone mass of the TiO_2@UCN/Qr/LA + group is larger than those of the Ti, Ti +, and TiO_2@UCN/Qr/LA groups. The corresponding quantitative analysis (Fig. 9B and C) reveals that the new bone mass of the TiO_2@UCN/Qr/LA + group is the biggest with the bone volume (BV) being 4.19 and bone volume/total volume (BV/TV) being 40.58. The TiO_2@UCN/Qr/LA group fares slightly better than the Ti and Ti + groups perhaps due to the nanostructure and Qr. Furthermore, osteogenic or cartilage differentiation on the implants is analyzed by Safranin-O and Fast Green staining. Fig. 9D shows plenty of new dense bone around the TiO_2@UCN/Qr/LA + implant and it is confirmed by H&E staining (Fig. 9E), indicating TiO_2@UCN/Qr/LA + implant promotes osseointegration. The increased amount of new bone on TiO_2@UCN/Qr/LA + in the presence of biofilms infection is ascribed to the anti-infection and osteogenic ability.

Finally, histological analysis is conducted on the main organs including the heart, liver, spleen, lung, and kidney by H&E staining to investigate the bio-safety of TiO_2@UCN/Qr/LA. No obvious toxicity or damage to the main organs is observed (Figure S19) thereby corroborating the biological safety.

4. Conclusion

An NIR-II-triggered multifunctional nano-platform is designed for Ti implants to ablate osteosarcoma, eliminate biofilms, and promote osseointegration at the same time. The TiO_2 nano-shovel shows the photothermal ability and doping with Yb and Er leads to excellent photocatalytic performance under 1,060 nm laser irradiation. The ROS generated catalyze LA to produce NO. Systematic *in vitro* and *in vivo* assessments verify the ability of TiO_2@UCN/Qr/LA to ablate tumors and eliminate biofilms as a result of the combined effects of PTT, PDT, Qr

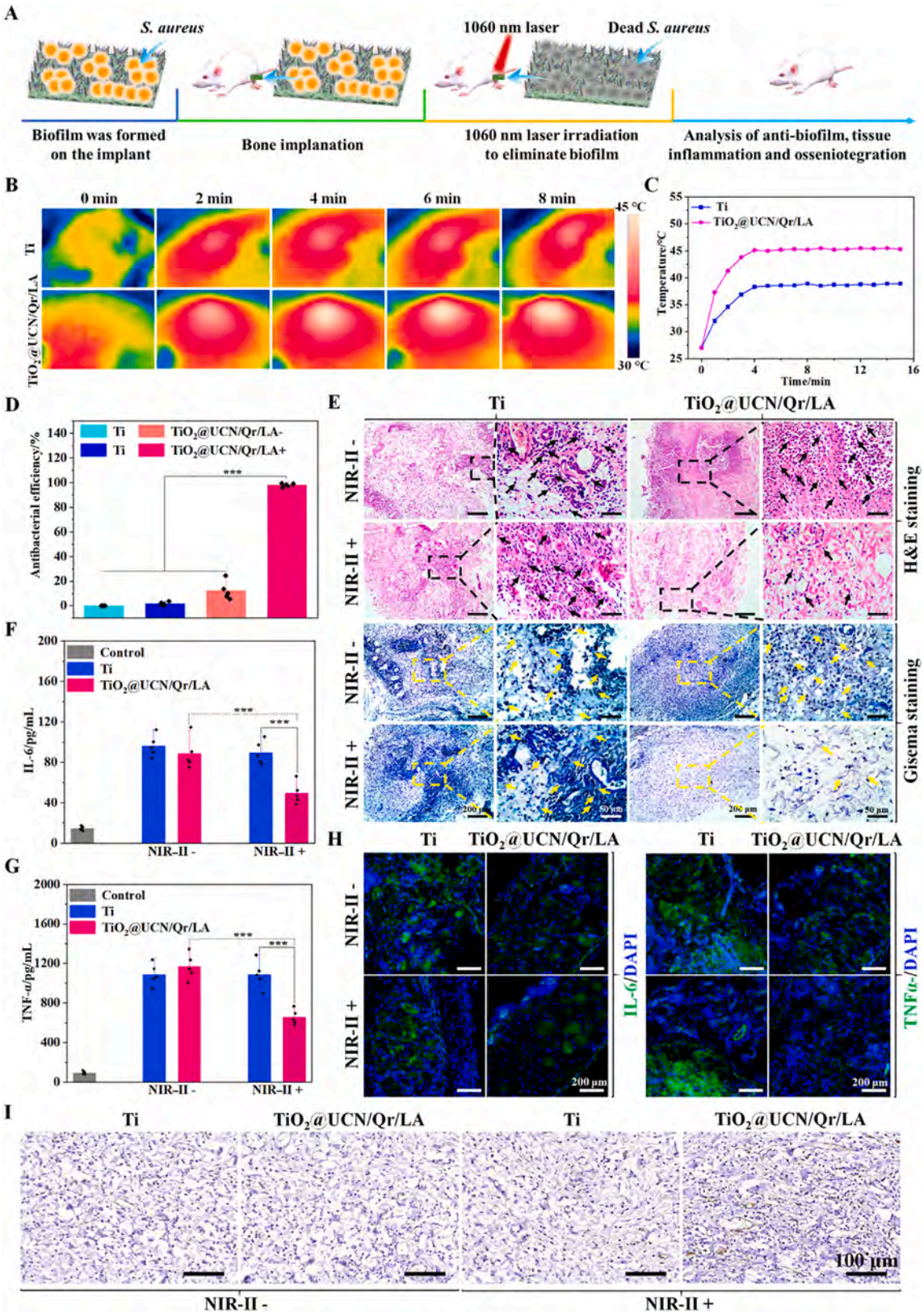

Fig. 8. *In vivo* evaluation of anti-biofilm and anti-inflammation effects: (A) The schematic diagram of TiO_2@UCN/Qr/LA for anti-biofilm and osseointegration testing; (B) Infrared images and (C) Heating curves of the Ti and TiO_2@UCN/Qr/LA groups at the implant sites irradiation with the 1,060 nm laser (0.6 W cm^{-2}); (D) Anti-biofilm efficiency of the Ti, Ti +, TiO_2@UCN/Qr/LA, and TiO_2@UCN/Qr/LA + groups in mice; (E) H&E and Giemsa staining of soft tissues surrounding the implants after two days with the black and yellow arrows indicating neutrophils and bacteria, respectively; (F) and (G) ELISA detection of inflammation markers (IL-6 and TNF-α) of the tissues surrounding the implants; (H) Immunofluorescence staining images of IL-6 and TNF-α *in vivo*; (I) CD31 immunohistochemistry of soft tissues surrounding the implants (***$p < 0.001$).

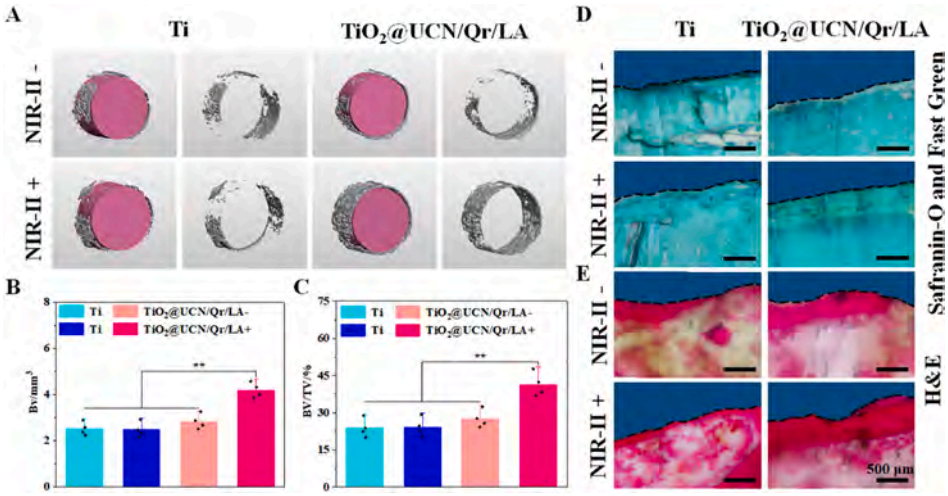

Fig. 9. Bone formation evaluation *in vivo*: (A) 3D micro-CT reconstructed images of the Ti, Ti +, TiO_2@UCN/Qr/LA, and TiO_2@UCN/Qr/LA + groups; (B) Quantitative analysis of BV, (C) BV/TV, (D) Safranin-O and Fast Green, and (E) H&E staining of the tissues around the implants (**$p < 0.01$).

and NO. NO also facilitates angiogenesis and combined with the anti-inflammatory ability and osteogenic differentiation rendered by Qr, osseointegration is promoted.

Declaration of Competing Interest

The authors declare that they have no known competing financial interests or personal relationships that could have appeared to influence the work reported in this paper.

Acknowledgements

This work was supported by the National Natural Science Foundation of China (31700834, 11632013, 81772867 and 81902273), Post-doctoral Science Foundation of China (2021 M691992), Major Projects in Research and Development of Shanxi (Projects of International Cooperation, 201803D421090 and 201803D421066), Fund for Shanxi "1331 Project" Key Innovative Research Team (PY201809), Scientific Research Project in Second Hospital of Shanxi Medical University (202002-4), Natural Science Foundation of Jiangsu Province Special Equipment Safety Supervision Inspection Institute (KJ(Y)2020037), and Guangdong - Hong Kong Technology Cooperation Funding Scheme (TCFS) GHP/085/18SZ (CityU 9440230).

Appendix A. Supplementary data

Supplementary data to this article can be found online at https://doi.org/10.1016/j.cej.2021.131155.

References

[1] N. Rainusso, L.L. Wang, J.T. Yustein, The adolescent and young adult with cancer: State of the art-bone tumors, Curr. Oncol. Rep. 15 (4) (2013) 296–307.
[2] M. Kansara, M.W. Teng, M.J. Smyth, D.M. Thomas, Translational biology of osteosarcoma, Nat. Rev. Canc. 14 (11) (2014) 722–735.
[3] W.Q. Chen, R.S. Zheng, P.D. Baade, S.W. Zhang, H.M. Zeng, F. Bray, A. Jemal, Q. Y. Xue, H. Jie, Cancer statistics in China, CA-Cancer, J. Clin. 66 (2016) (2015) 115–132.
[4] M.S. Isakoff, S.S. Bielack, P. Meltzer, R. Gorlick, Osteosarcoma: Current treatment and a collaborative pathway to success, J. Clin. Oncol. 33 (2015) 3029–3035.
[5] A. Italiano, O. Mir, A. Cioffi, E. Palmerini, S. Piperno-Neumann, C. Perrin, L. Chaigneau, N. Penel, F. Duffaud, J.E. Kurtz, O. Collard, F. Bertucci, E. Bompas, A. Le Cesne, R.G. Maki, I. Ray Coquard, J.Y. Blay, Advanced chondrosarcomas: Role of chemotherapy and survival, Ann. Oncol. 24 (2013) 2916–2922.
[6] J.S. Whelan, L.E. Davis, Osteosarcoma, chondrosarcoma, and chordoma, J. Clin. Oncol. 36 (2) (2018) 188–193.
[7] R.K. Heck, T.D. Peabody, M.A. Simon, Staging of primary malignancies of bone, Ca-Cancer J. Clin. 56 (6) (2006) 366–375.
[8] A. Luetke, P.A. Meyers, I. Lewis, H. Juergens, Osteosarcoma treatment -Where do we stand? A state of the art review, Cancer Treat. Rev. 40 (4) (2014) 523–532.
[9] H. Ma, C. Jiang, D. Zhai, Y. Luo, Y. Chen, F. Lv, Z. Yi, Y. Deng, J. Wang, J. Chang, C. Wu, A bifunctional biomaterial with photothermal effect for tumor therapy and bone regeneration, Adv. Funct. Mater. 26 (2016) 1197–1208.
[10] J. Tan, M. Zhang, Z. Hai, C. Wu, J. Lin, W. Kuang, H. Tang, Y. Huang, X. Chen, G. Liang, Sustained release of two bioactive factors from supramolecular hydrogel promotes periodontal bone regeneration, ACS Nano 13 (5) (2019) 5616–5622.
[11] K. Zhou, P. Yu, X. Shi, T. Ling, W. Zeng, A. Chen, W. Yang, Z. Zhou, Hierarchically porous hydroxyapatite hybrid scaffold incorporated with reduced graphene oxide for rapid bone ingrowth and repair, ACS Nano 13 (2019) 9595–9606.
[12] C.A. Stiller, A. Trama, D. Serraino, S. Rossi, C. Navarro, M.D. Chirlaque, P. G. Casali, Descriptive epidemiology of sarcomas in Europe: Report from the RARECARE project, Eur. J. Cancer 49 (2013) 684–695.
[13] E. Verron, H. Schmid-Antomarchi, H. Pascal-Mousselard, A. Schmid-Alliana, J.-C. Scimeca, J.-M. Bouler, Therapeutic strategies for treating osteolytic bone metastases, Drug Discovery Today 19 (9) (2014) 1419–1426.
[14] F.D. Lowy, J. Clin, Antimicrobial resistance: The example of staphylococcus aureus, Invest. 111 (2013) 1265–1273.
[15] Y. Liu, H.J. Busscher, B. Zhao, Y. Li, Z. Zhang, H.C. van der Mei, Y. Ren, L. Shi, Surface-adaptive, antimicrobially loaded, micellar nanocarriers with enhanced penetration and killing efficiency in staphylococcal biofilms, ACS Nano 10 (4) (2016) 4779–4789.
[16] J. Xie, H. Zhang, S. Li, R. Wang, X. Sun, M. Zhou, J. Zhou, X.W. Lou, Y. Xie, Defect-rich MoS_2 ultrathin nanosheets with additional active edge sites for enhanced electrocatalytic hydrogen evolution, Adv. Mater. 25 (2013) 5807–5813.
[17] Z. Yuan, B. Tao, Y. He, J. Liu, K. Cai, Biocompatible MoS_2/PDA-RGD coating on titanium implant with antibacterial property via intrinsic ROS-independent oxidative stress and Nir irradiation, Biomaterials 217 (2019), 119290.
[18] H.J. Xiang, Q.H. Yang, Y.S. Gao, D.Y. Zhu, S.S. Pan, T.M. Xu, Y. Chen, Cocrystal strategy toward multifunctional 3D-printing scaffolds enables NIR-activated photonic osteosarcoma hyperthermia and enhanced bone defect regeneration, Adv. Funct. Mater. 30 (2020) 1909938.
[19] Z. Zhang, J. Wang, C. Chen, Near-infrared light-mediated nanoplatforms for cancer thermo-chemotherapy and optical imaging, Adv. Mater. 25 (28) (2013) 3869–3880.
[20] P. Hu, T. Wu, W. Fan, L. Chen, Y. Liu, D. Ni, W. Bu, J. Shi, Near infrared-assisted fenton reaction for tumor-specific and mitochondrial dna-targeted photochemotherapy, Biomater. 141 (2017) 86–95.
[21] Y. Li, X. Liu, L. Tan, Z. Cui, X. Yang, Y. Zheng, K.W.K. Yeung, P.K. Chu, S. Wu, Rapid sterilization and accelerated wound healing using Zn^{2+} and graphene oxide modified g-C_3N4 under dual light irradiation, Adv. Funct. Mater. 28 (2018) 1800299.
[22] G. Hong, A.L. Antaris, H. Dai, Near-infrared fluorophores for biomedical imaging, Nat. Biomed. Eng. 1 (2017) 1–22.
[23] Y. Jiang, K. Pu, Molecular fluorescence and photoacoustic imaging in the second near-infrared optical window using organic contrast agents, Adv. Biosyst. 2 (2018) 1700262.
[24] S. Lal, S.E. Clare, N.J. Halas, Nanoshell-enabled photothermal cancer therapy: Impending clinical impact, Acc. Chem. Res. 41 (12) (2008) 1842–1851.
[25] K. Yang, L. Feng, X. Shi, Z. Liu, Nano-graphene in biomedicine: Theranostic applications, Chem. Soc. Rev. 42 (2) (2013) 530–547.
[26] G. Zhang, X. Zhang, Y. Yang, R. Chi, J. Shi, R. Hang, X. Huang, X. Yao, P.K. Chu, X. Zhang, Dual light-induced in situ antibacterial activities of biocompatibleTiO_2/MoS_2/PDA/RGD nanorod arrays on titanium, Biomater. Sci. 8 (1) (2020) 391–404.
[27] L. Tan, J. Li, X. Liu, Z. Cui, X. Yang, S. Zhu, Z. Li, X. Yuan, Y. Zheng, K.W.K. Yeung, H. Pan, X. Wang, S. Wu, Rapid biofilm eradication on bone implants using red phosphorus and near-infrared light, Adv. Mater. 30 (2018) 1801808.

[28] D.E.J.G.J. Dolmans, D. Fukumura, R.K. Jain, Photodynamic Therapy for Cancer, Nat. Rev. Cancer 3 (5) (2003) 380–387.
[29] L.D. Yu, P. Hu, Y. Chen, Gas-generating nanoplatforms: Material chemistry, multifunctionality, and gas therapy, Adv. Mater. 30 (2018) 1801964.
[30] J. Yao, Y. Liu, J. Wang, Q. Jiang, D. She, H. Guo, N. Sun, Z. Pang, C. Deng, W. Yang, S. Shen, On-demand CO release for amplification of chemotherapy by MOF functionalized magnetic carbon nanoparticles with NIR irradiation, Biomaterials 195 (2019) 51–62.
[31] H. Lin, Y. Chen, J. Shi, Nanoparticle-triggered in situ catalytic chemical reactions for tumour-specific therapy, Chem. Soc. Rev. 47 (6) (2018) 1938–1958.
[32] A.C. Midgley, Y. Wei, Z. Li, D. Kong, Q. Zhao, Nitric-oxide-releasing biomaterial regulation of the stem cell microenvironment in regenerative medicine, Adv. Mater. 32 (2020) 1805818.
[33] C.-H. Su, W.-P. Li, L.-C. Tsao, L.-C. Wang, Y.-P. Hsu, W.-J. Wang, M.-C. Liao, C.-L. Lee, C.-S. Yeh, Enhancing microcirculation on multitriggering manner facilitates angiogenesis and collagen deposition on wound healing by photoreleased NO from hemin-derivatized colloids, ACS Nano 13 (4) (2019) 4290–4301.
[34] S. Sortino, Light-controlled nitric oxide delivering molecular assemblies, Chem. Soc. Rev. 39 (8) (2010) 2903.
[35] X. Zhang, J. Du, Z. Guo, J. Yu, Q. Gao, W. Yin, S. Zhu, Z. Gu, Y. Zhao, Efficient near infrared light triggered nitric oxide release nanocomposites for sensitizing mild photothermal therapy, Adv. Sci. 6 (2018) 1801122.
[36] J. Fan, N. He, Q. He, Y. Liu, Y. Ma, X. Fu, Y. Liu, P. Huang, X. Chen, A novel self-assembled sandwich nanomedicine for NIR-responsive release of NO, Nanoscale 7 (47) (2015) 20055–20062.
[37] J. Xu, F. Zeng, H. Wu, C. Hu, C. Yu, S. Wu, Preparation of a mitochondria-targeted and NO-releasing nanoplatform and its enhanced pro-apoptotic effect on cancer cells, Small 10 (18) (2014) 3750–3760.
[38] D. Wink, K. Kasprzak, C. Maragos, R. Elespuru, M. Misra, T. Dunams, T. Cebula, W. Koch, A. Andrews, J. Allen, DNA deaminating ability and genotoxicity of nitric oxide and its progenitors, Science 254 (1991) 1001–1003.
[39] E.M. Hetrick, J.H. Shin, N.A. Stasko, C.B. Johnson, D.A. Wespe, E. Holmuhamedov, M.H. Schoenfisch, Bactericidal efficacy of nitric oxide-releasing silica nanoparticles, ACS Nano 2 (2) (2008) 235–246.
[40] D.D. Roberts, J.S. Isenberg, L.A. Ridnour, D.A. Wink, Nitric oxide and its gatekeeper thrombospondin-1 in tumor angiogenesis, Clin. Cancer Res. 13 (2007) 795–798.
[41] L.A. Ridnour, J.S. Isenberg, M.G. Espey, D.D. Thomas, D.D. Roberts, D.A. Wink, Nitric oxide regulates angiogenesis through a functional switch involving thrombospondin-1, Proc. Natl. Acad. Sci. USA 102 (37) (2005) 13147–13152.
[42] M. De Ridder, D. Verellen, V. Verovski, G. Storme, Hypoxic tumor cell radiosensitization through nitric oxide, Nitric Oxide 19 (2008) 164–169.
[43] H.-J. Xiang, Q. Deng, L. An, M. Guo, S.-P. Yang, J.-G. Liu, Tumor cell specific and lysosome-targeted delivery of nitric oxide for enhanced photodynamic therapy triggered by 808 nm near-infrared light, Chem. Commun. 52 (1) (2016) 148–151.
[44] J.B. Dattilo, R.G. Makhoul, The role of nitric oxide in vascular biology and pathobiology, Ann. Vasc. Surg. 11 (1997) 307–314.
[45] X. Zhang, G. Tian, W. Yin, L. Wang, X. Zheng, L. Yan, J. Li, H. Su, C. Chen, Z. Gu, Y. Zhao, Controllable generation of nitric oxide by near-infrared-sensitized upconversion nanoparticles for tumor therapy, Adv. Funct. Mater. 25 (20) (2015) 3049–3056.
[46] M.M. Wan, H. Chen, Q. Wang, Q. Niu, P. Xu, Y.Q. Yu, T.Y. Zhu, C. Mao, J. Shen, Bio-inspired nitric-oxide-driven nanomotor, Nat. Commun. 10 (2019) 1–11.
[47] S.S. Wan, J.Y. Zeng, H. Cheng, X.Z. Zhang, ROS-induced NO generation for gas therapy and sensitizing photodynamic therapy of tumor, Biomaterials 185 (2018) 51–62.
[48] D. Amić, D. Davidović-Amić, D. Bešlo, V. Rastija, B. Lučić, N. Trinajstić, SAR and QSAR of the antioxidant activity of flavonoids, Curr. Med. Chem. 14 (2007) 827–845.
[49] S. Srivastava, R. Bankar, P. Roy, Assessment of the role of flavonoids for inducing osteoblast differentiation in isolated mouse bone marrow derived mesenchymal stem cells, Phytomedicine 20 (8-9) (2013) 683–690.
[50] A. Córdoba, M. Satué, M. Gómez-Florit, M. Hierro-Oliva, C. Petzold, S. P. Lyngstadaas, M.L. González-Martín, M. Monjo, J.M. Ramis, Flavonoid-modified surface: Multifunctional bioactive biomaterials with osteopromotive, anti-inflammatory, and anti-fibrotic potential, Adv. Healthcare Mater. 4 (2015) 540–549.
[51] Z. Yuan, C. Lin, Y. He, B. Tao, M. Chen, J. Zhang, P. Liu, K. Cai, Near-Infrared light-triggered nitric-oxide-enhanced photodynamic therapy and low-temperature photothermal therapy for biofilm elimination, ACS Nano 14 (3) (2020) 3546–3562.
[52] P. Li, C. Zhou, S. Rayatpisheh, K. Ye, Y.F. Poon, P.T. Hammond, H. Duan, M. B. Chan-Park, Cationic peptidopolysaccharides show excellent broad-spectrum antimicrobial activities and high selectivity, Adv. Mater. 24 (30) (2012) 4130–4137.
[53] C.H. Kim, M.S. Khil, H.Y. Kim, H.U. Lee, K.Y. Jahng, An improved hydrophilicity via electrospinning for enhanced cell attachment and proliferation, J. Biomed. Mater. Res., Part B 78 (2006) 283–290.
[54] X. Zhang, G. Zhang, M. Chai, X. Yao, W. Chen, P.K. Chu, Synergistic antibacterial activity of physical-chemical multi-mechanism by TiO_2 nanorod arrays for safe biofilm eradication on implant, Bioact. Mater. 6 (1) (2021) 12–25.
[55] G.N. Zhang, Y.Q. Yang, J. Shi, X.H. Yao, W.Y. Chen, X.C. Wei, X.Y. Zhang, P.K. Chu, Near-Infrared Light II - Assisted Rapid Biofilm Elimination Platform for Bone Implants at Mild Temperature, Biomaterials 269 (2021), 120634.
[56] T. Csizmadia, M. Erdélyi, T. Smausz, T. Novák, B. Hopp, Simulation of the reflectivity properties of microstructured titanium surface by ray tracing method, J. Laser Micro Nanoen. 10 (2) (2015) 210–215.
[57] X.J. Gong, X.F. Gao, L. Jiang, Recent progress in bionic condensate microdrop selfpropelling surfaces, Adv. Mater. 29 (2017) 1703002.
[58] J. Zhu, Y. Luo, J. Tian, J. Li, X. Gao, Clustered ribbed-nanoneedle structured copper surfaces with high-efficiency dropwise condensation heat transfer performance, ACS Appl. Mater. Interfaces 7 (20) (2015) 10660–10665.
[59] J. Zhou, P. Luo, C. Sun, L.C. Meng, S.S. Chen, H.C. Yao, B. Du, A "win-win" nanoplatform TiO2:Yb Ho, F for NIR light-induced synergistic therapy and imaging, Nanoscale 9 (2017) 4244–4254.
[60] W. Wang, Q. Shang, W. Zheng, H. Yu, X. Feng, Z. Wang, Y. Zhang, G. Li, A novel near-infrared antibacterial material depending on the upconverting property of Er^{3+}-Yb^{3+}-Fe^{3+} tridoped TiO_2 nanopowder, J. Phys. Chem. C 114 (32) (2010) 13663–13669.
[61] J. Choi, H. Park, M.R. Hoffmann, Effects of single metal-ion doping on the visible-light photoreactivity of TiO_2, J. Phys. Chem. C 114 (2) (2010) 783–792.
[62] J.I. Brauer, G. Szulczewski, Important role of surface fluoride in nitrogen-doped TiO2 nanoparticles with visible light photocatalytic activity, J. Phys. Chem. B 118 (2014) 14188–14195.
[63] Z. He, W. Que, J. Chen, X. Yin, Y. He, J. Ren, Photocatalytic degradation of methyl orange over nitrogen-fluorine codoped TiO_2 nanobelts prepared by solvothermal synthesis, ACS Appl. Mater. Interfaces 4 (12) (2012) 6816–6826.
[64] Q. Zhang, X. Liu, L. Tan, Z. Cui, Z. Li, Y. Liang, S. Zhu, K.W.K. Yeung, Y. Zheng, S. Wu, An UV to NIR-driven platform based on red phosphorus/graphene oxide film for rapid microbial inactivation, Chem. Eng. J. 383 (2020) 123088.
[65] L. Ma, X. Feng, H. Liang, K. Wang, Y. Song, L. Tan, B. Wang, R. Luo, Z. Liao, G. Li, X. Liu, S. Wu, C. Yang, A novel photothermally controlled multifunctional scaffold for clinical treatment of osteosarcoma and tissue regeneration, Mater. Today 36 (2020) 48–62.
[66] P. Wen, M.-H. Zong, T.-G. Hu, L. Li, H. Wu, Preparation and characterization of electrospun colon-specific delivery system for quercetin and its antiproliferative effect on cancer cells, J. Agric. Food Chem. 66 (44) (2018) 11550–11559.
[67] K. Hu, L. Miao, T.J. Goodwin, J. Li, Q. Liu, L. Huang, Quercetin remodels the tumor microenvironment to improve the permeation, retention, and antitumoreffects of nanoparticles, ACS Nano 11 (5) (2017) 4916–4925.
[68] M. Yousuf, P. Khan, A. Shamsi, M. Shahbaaz, G.M. Hasan, Q.M.R. Haque, A. Christoffels, A. Islam, M.I. Hassan, Inhibiting CDK6 activity by quercetin is an attractive strategy for cancer therapy, ACS Omega 5 (42) (2020) 27480–27491.
[69] H.-J. Kim, S.-K. Kim, B.-S. Kim, S.-H. Lee, Y.-S. Park, B.-K. Park, S.-J. Kim, J. Kim, C. Choi, J.-S. Kim, S.-D. Cho, J.-W. Jung, K.-H. Roh, K.-S. Kang, J.-Y. Jung, Apoptotic effect of quercetin on HT-29 colon cancer cells via the AMPK signaling pathway, J. Agric. Food Chem. 58 (15) (2010) 8643–8650.
[70] T.C. Ma, Y.D. Liu, Q. Wu, L.F. Luo, Y.L. Cui, X.H. Wang, X.W. Chen, L.F. Tan, X.W. Meng, Quercetin-modified metal−organic frameworks for dual sensitization of radiotherapy in tumor tissues by inhibiting the carbonic anhydrase IX, ACS Nano 13 (2019) 4209-4219.
[71] J. Zhang, L. Shen, X. Li, W. Song, Y. Liu, L. Huang, Nanoformulated codelivery of quercetin and alantolactone promotes an antitumor response through synergistic immunogenic cell death for microsatellite-stable colorectal cancer, ACS Nano 13 (11) (2019) 12511–12524.
[72] H.C. Flemming, J. Wingender, U. Szewzyk, P. Steinberg, S.A. Rice, S. Kjelleberg, Biofilms: An emergent form of bacterial life, Nat. Rev. Microbiol. 14 (2016) 563–575.
[73] Y. Liu, L. Shi, L. Su, H.C. van der Mei, P.C. Jutte, Y. Ren, H.J. Busscher, Nanotechnology-based antimicrobials and delivery systems for biofilm-infection control, Chem. Soc. Rev. 48 (2) (2019) 428–446.
[74] L. Sun, W. Jiang, H. Zhang, Y. Guo, W. Chen, Y. Jin, H. Chen, K. Du, H. Dai, J. Ji, B. Wang, Photosensitizer-loaded multifunctional chitosan nanoparticles for simultaneous in situ imaging, highly efficient bacterial biofilm eradication, and tumor ablation, ACS Appl. Mater. Interfaces 11 (2) (2019) 2302–2316.
[75] D. Hu, Y. Deng, F. Jia, Q. Jin, J. Ji, Surface charge switchable supramolecular nanocarriers for nitric oxide synergistic photodynamic eradication of biofilms, ACS Nano 14 (1) (2020) 347–359.
[76] C. Szabó, H. Ischiropoulos, R. Radi, Peroxynitrite: Biochemistry, pathophysiology and development of therapeutics, Nat. Rev. Drug Discov. 6 (8) (2007) 662–680.
[77] D. Wang, L. Niu, Z.-Y. Qiao, D.-B. Cheng, J. Wang, Y. Zhong, F. Bai, H. Wang, H. Fan, Synthesis of self-assembled porphyrin nanoparticle photosensitizers, ACS Nano 12 (4) (2018) 3796–3803.
[78] A.M.L. Hossion, Y. Zamami, R.K. Kandahary, T. Tsuchiya, W. Ogawa, A. Iwado, K. Sasaki, Quercetin diacylglycoside analogues showing dual inhibition of DNA gyrase and topoisomerase IV as novel antibacterial agents, J. Med. Chem. 54 (11) (2011) 3686–3703.
[79] F.A. Ramos, Y. Takaishi, M. Shirotori, Y. Kawaguchi, K. Tsuchiya, H. Shibata, T. Higuti, T. Tadokoro, M. Takeuchi, Antibacterial and antioxidant activities of quercetin oxidation products from yellow onion (allium cepa) skin, J. Agric. Food Chem. 54 (10) (2006) 3551–3557.
[80] S. Ahmad, P.W. Hewett, P. Wang, B. Al-Ani, M. Cudmore, T. Fujisawa, J.J. Haigh, F. le Noble, L. Wang, D. Mukhopadhyay, A. Ahmed, Direct evidence for endothelial vascular endothelial growth factor receptor-1 function in nitric oxideemediated angiogenesis, Circ. Res. 99 (2006) 715–722.
[81] U.H. Langen, M.E. Pitulescu, J.M. Kim, R. Enriquez-Gasca, K.K. Sivaraj, A. Kusumbe, A. Singh, J. Di Russo, M.G. Bixel, B. Zhou, L. Sorokin, J. Vaquerizas, R.H. Adams, Cell-matrix signals specify bone endothelial cells during developmental osteogenesis, Nat. Cell Biol. 19 (3) (2017) 189–201.
[82] D.A. Greenberg, K. Jin, From angiogenesis to neuropathology, Nature 438 (2005) 954e959.
[83] C.H. Su, W.P. Li, L.C. Tsao, L.C. Wang, Y.P. Hsu, W.J. Wang, M.C. Liao, C.L. Lee, C. S. Yeh, Enhancing microcirculation on multitriggering manner facilitates

angiogenesis and collagen deposition on wound healing by photoreleased NO from hemin-derivatized colloids, ACS Nano 13 (2019) 4290–4301.
[84] M.M. Wan, H. Chen, Q. Wang, Q. Niu, P. Xu, Y.Q. Yu, T.Y. Zhu, C. Mao, J. Shen, Bio-inspired nitric-oxide-driven nanomotor, Nat. Commun. 10 (2019) 966.
[85] S.K. Ramasamy, A.P. Kusumbe, L. Wang, R.H. Adams, Endothelial Notch activity promotes angiogenesis and osteogenesis in bone, Nature 507 (2014) 376–380.
[86] A.P. Kusumbe, S.K. Ramasamy, R.H. Adams, Coupling of angiogenesis and osteogenesis by a specific vessel subtype in bone, Nature 507 (2014) 323–328.
[87] W. Zhang, Z. Li, Q. Huang, L. Xu, J. Li, Y. Jin, G. Wang, X. Liu, X. Jiang, Effects of a hybrid micro/nanorod topography-modified titanium implant on adhesion and osteogenic differentiation in rat bone marrow mesenchymal stem cells, Int. J. Nanomed. 8 (2013) 257–265.
[88] X. Liu, S. Wang, Three-dimensional nano-biointerface as a new platform for guiding cell fate, Chem. Soc. Rev. 43 (8) (2014) 2385–2401.
[89] L. Richert, F. Vetrone, J.-H. Yi, S.F. Zalzal, J.D. Wuest, F. Rosei, A. Nanci, Surface nanopatterning to control cell growth, Adv. Mater. 20 (8) (2008) 1488–1492.
[90] R.A. Gittens, R. Olivares-Navarrete, Z. Schwartz, B.D. Boyan, Implant osseointegration and the role of microroughness and nanostructures: Lessons for spine implants, Acta Biomater. 10 (8) (2014) 3363–3371.
[91] J. Sedo, J. Saiz-Poseu, F. Busque, D. Ruiz-Molina, Catechol-based biomimetic functional materials, Adv. Mater. 25 (2013) 653.
[92] F. Bensiamar, B. Olalde, S.C. Cifuentes, N. Argarate, G. Atorrasagasti, J. L. González-Carrasco, E. García-Rey, N. Vilaboa, L. Saldaña, Bioactivity of dexamethasone-releasing coatings on polymer/magnesium composites, Biomed. Mater. 11 (2016), 055011.
[93] J.M. Anderson, A. Rodriguez, D.T. Chang, Foreign body reaction to biomaterials, Semin. Immunol. 20 (2) (2008) 86–100.
[94] Z. Chen, T. Klein, R.Z. Murray, R. Crawford, J. Chang, C. Wu, Y. Xiao, Osteoimmunomodulation for the development of advanced bone biomaterials, Mater. Today 19 (6) (2016) 304–321.

Supplementary Information

A multifunctional antibacterial coating on bone implants for osteosarcoma therapy and enhanced osteointegration

Guannan Zhang[#a], Zhuangzhuang Wu[#b], Yongqiang Yang[c], Jing Shi[d], Jia Lv[b], Yi Fang[b], Zhen Shen[b], Zhi Lv**[b], Pengcui Li[b], Xiaohong Yao[a], Weiyi Chen[e], Xiaochun Wei[b], Paul K Chu[f], Xiangyu Zhang*[a,b,e]

[a] Laboratory of Biomaterial Surfaces & Interfaces, College of Materials Science and Engineering, Taiyuan University of Technology, Taiyuan 030024, China

[b] Shanxi Key Laboratory of Bone and Soft Tissue Injury Repair, Department of Orthopedics, Second Hospital of Shanxi Medical University, Taiyuan 030024, China

[c] Jiangsu Provinces Special Equipment Safety Supervision Inspection Institute, Branch of Wuxi, National Graphene Products Quality Supervision and Inspection Center, Jiangsu, Wuxi 214174, PR China

[d] Analytical Instrumentation Center, State Key Laboratory of Coal Conversion, Institute of coal chemistry, Chinese Academy of Sciences, Taiyuan 030001, China

[e] College of Biomedical Engineering, Taiyuan University of Technology, Taiyuan 030024, China

[f] Department of Physics, Department of Materials Science and Engineering, and Department of Biomedical Engineering, City University of Hong Kong, Tat Chee Avenue, Kowloon, Hong Kong, China

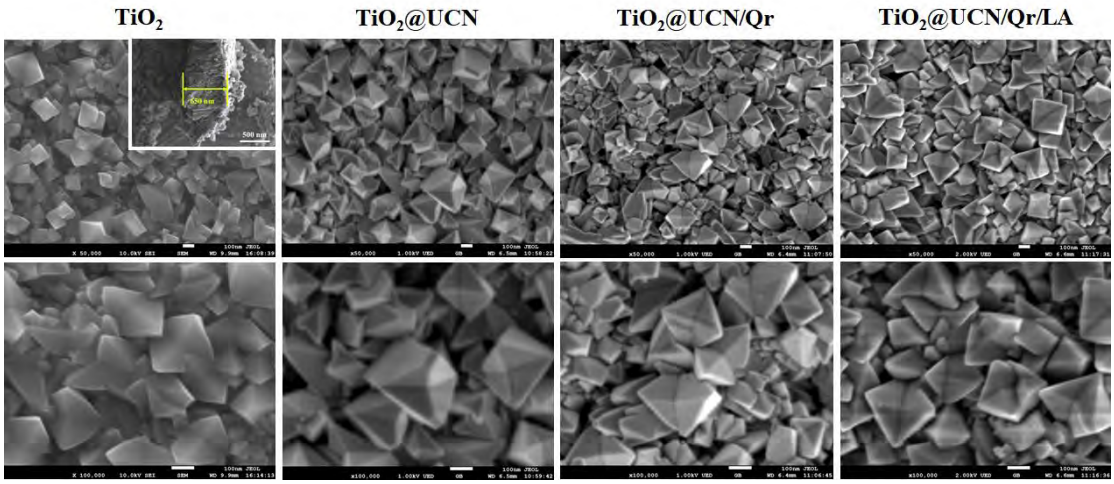

Figure S1. SEM images of TiO_2, TiO_2@UCN, TiO_2@UCN/Qr, and TiO_2@UCN/Qr/LA.

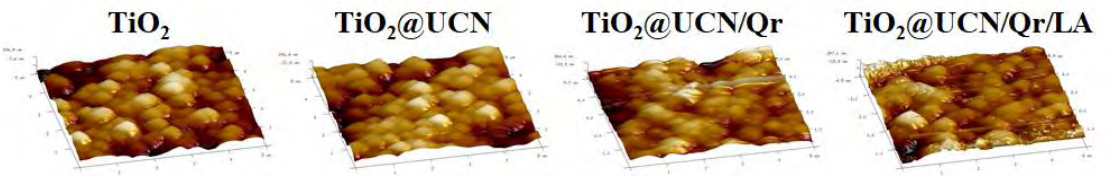

Figure S2. AFM images of TiO_2, TiO_2@UCN, TiO_2@UCN/Qr, and TiO_2@UCN/Qr/LA.

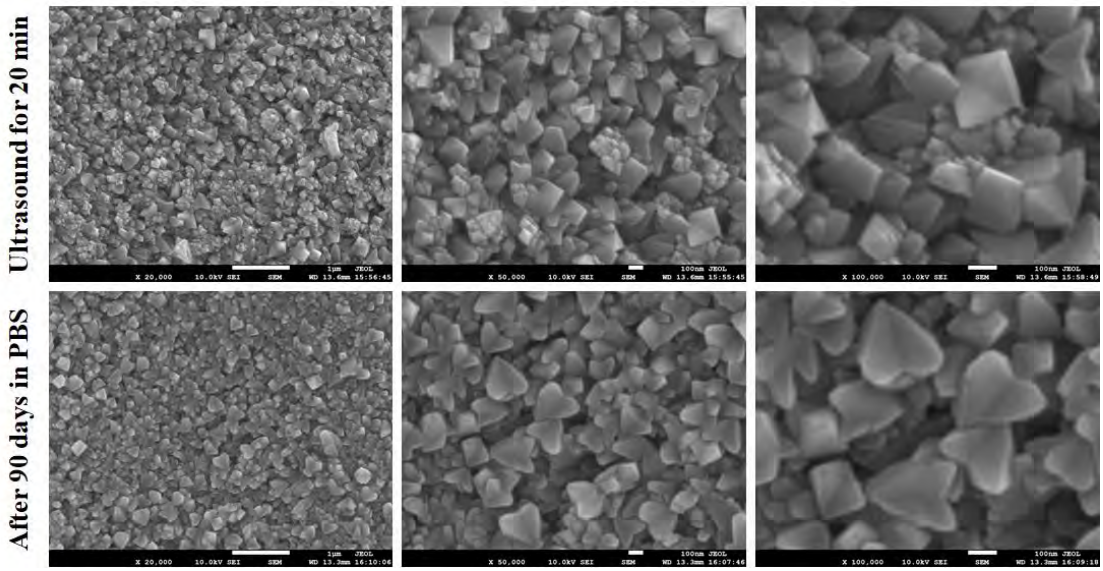

Figure S3. SEM images of TiO_2 after sonication for 20 min or immersion in PBS for 90 days at room temperature.

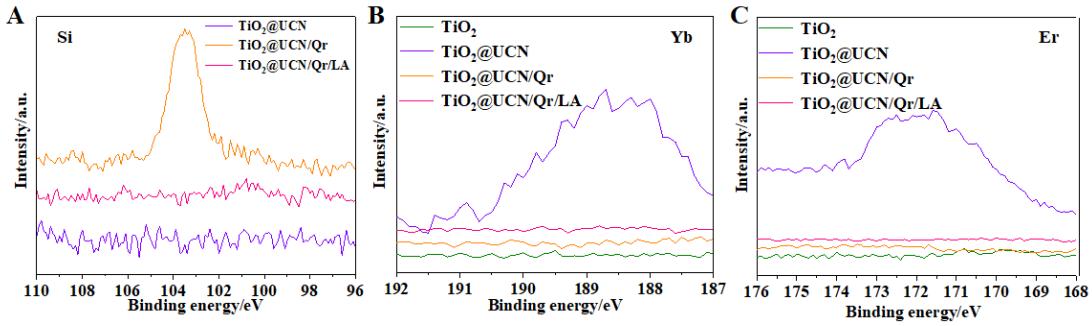

Figure S4. (A) High-resolution XPS Si 2p spectra of of TiO_2@UCN, TiO_2@UCN/Qr, and TiO_2@UCN/Qr/LA; (B) High-resolution Yb 4d spectra and (C) Er 4d spectra of TiO_2, TiO_2@UCN, TiO_2@UCN/Qr, and TiO_2@UCN/Qr/LA.

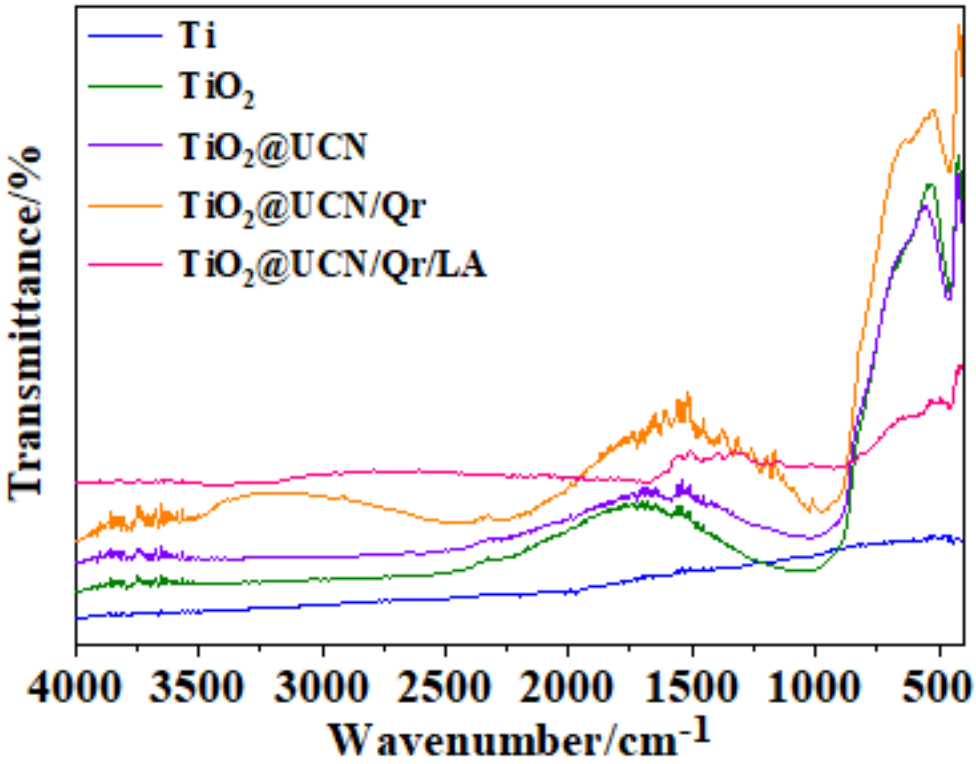

Figure S5. FTIR spectra of Ti, TiO_2, TiO_2@UCN, TiO_2@UCN/Qr, and TiO_2@UCN/Qr/LA.

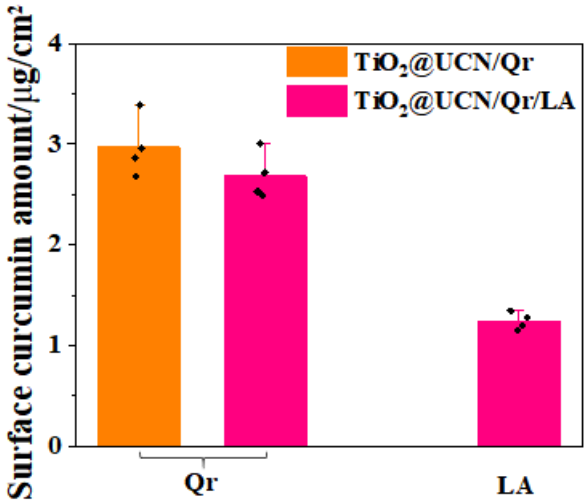

Figure S6. The amount of Qr on the surface of TiO_2@UCN/Qr and TiO_2@UCN/Qr/LA, and the amount of LA on the surface of TiO_2@UCN/Qr/LA.

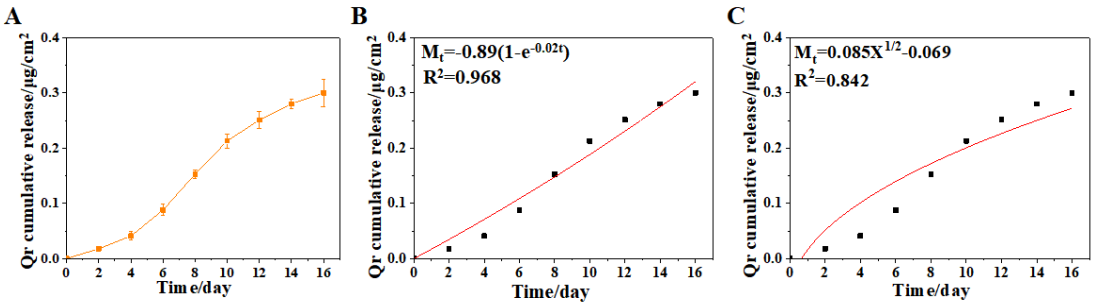

Figure S7. (A) The release curve of Qr on the surface of TiO_2@UCN/Qr/LA; (B) First-order model; (C) Higuchi model.

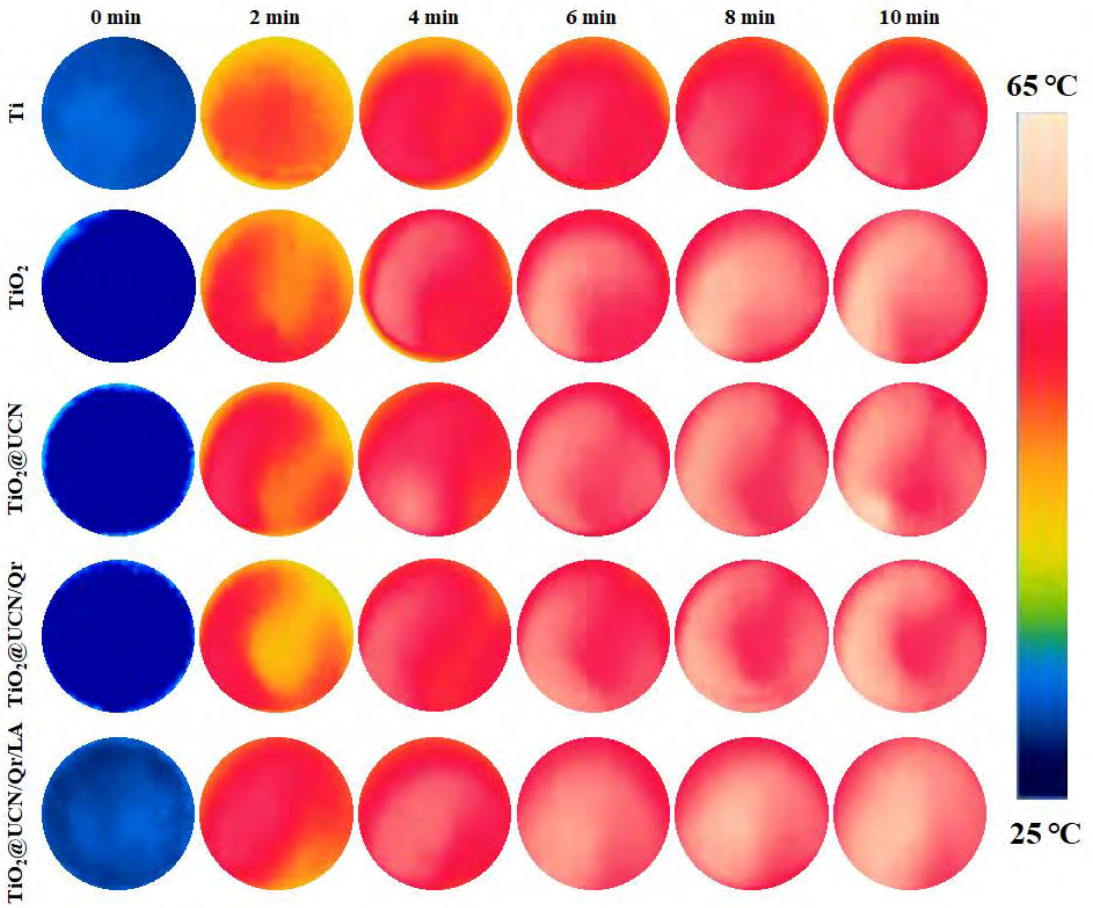

Figure S8. Photothermal images of Ti, TiO_2, TiO_2@UCN, TiO_2@UCN/Qr, and TiO_2@UCN/Qr/LA acquired at different time.

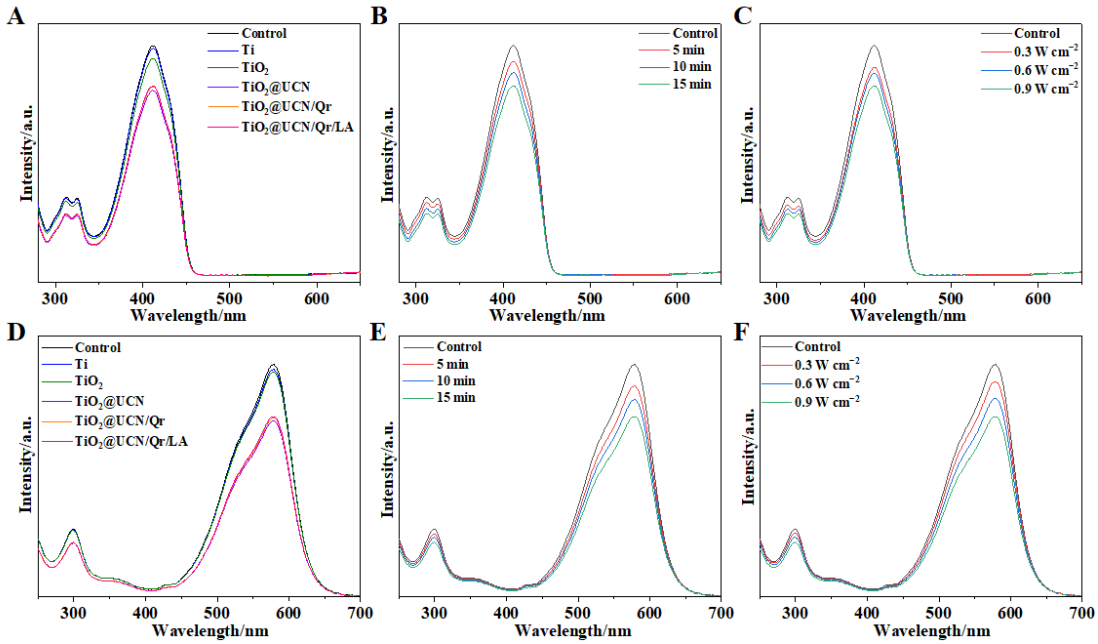

Figure S9. (A) $^1O_2$ spectra acquired during degradation of DPBF after 15 min (0.9 W cm^{-2}); $^1O_2$ spectra obtained during degradation of DPBF for TiO_2@UCN/Qr/LA at (B) different time and (C) different power density; (D) ·OH spectra showing decay of MV at 15 min (0.9 W cm^{-2}); ·OH spectra showing degradation of DPBF for TiO_2@UCN/Qr/LA at (E) different time and (F) different power density.

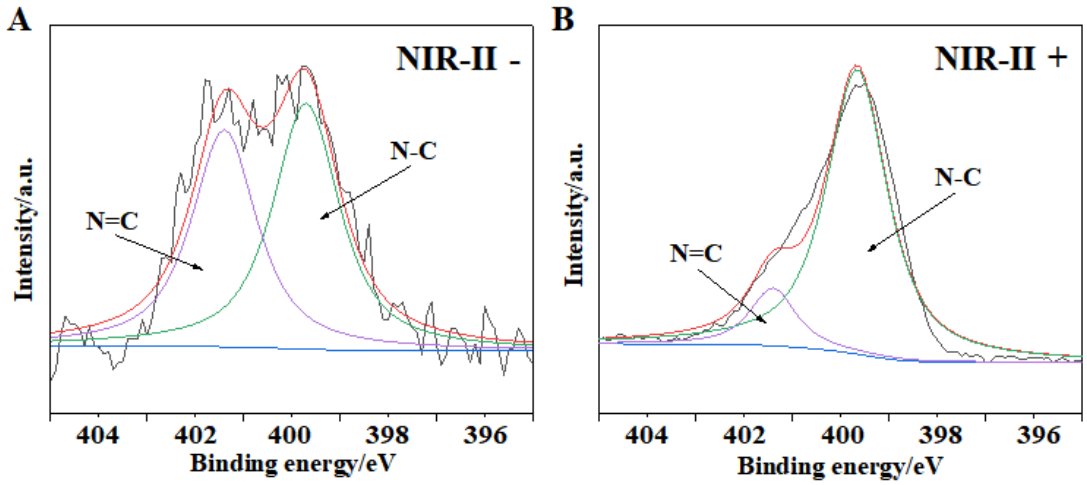

Figure S10. N 1s spectra of TiO_2@UCN/Qr/LA with or without 1060 nm laser irradiation.

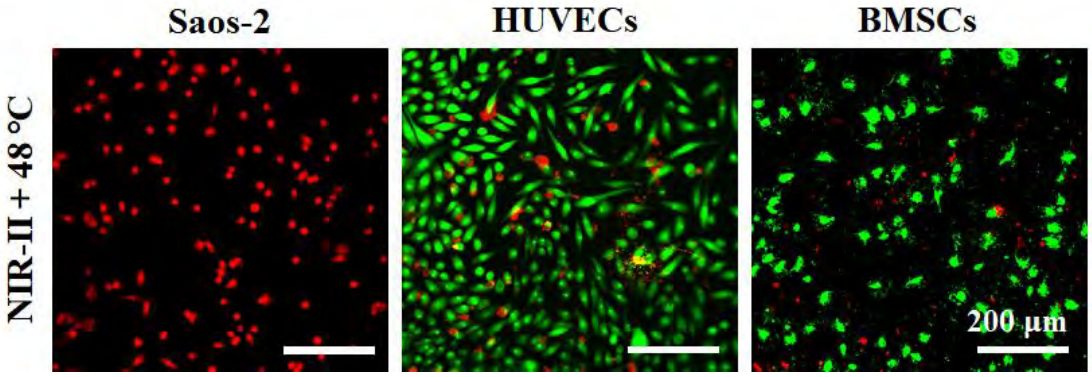

Figure S11. CLSM images of Saos-2, HUVECs, BMSCs cells (green/red represents live/dead cells).

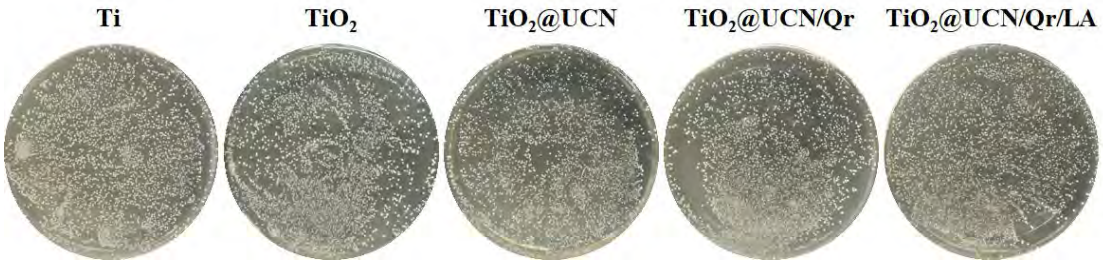

Figure S12. Photographs of *S. aureus* colonies detached from the biofilms under dark conditions after 15 min.

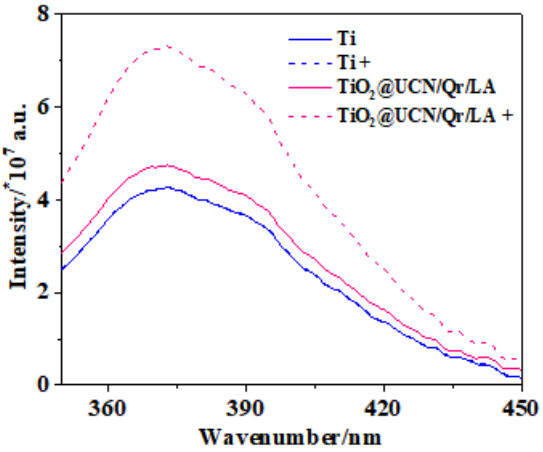

Figure S13. the relative ·ONOO- detection with an L-tyrosine probe after 1060 nm light irradiation.

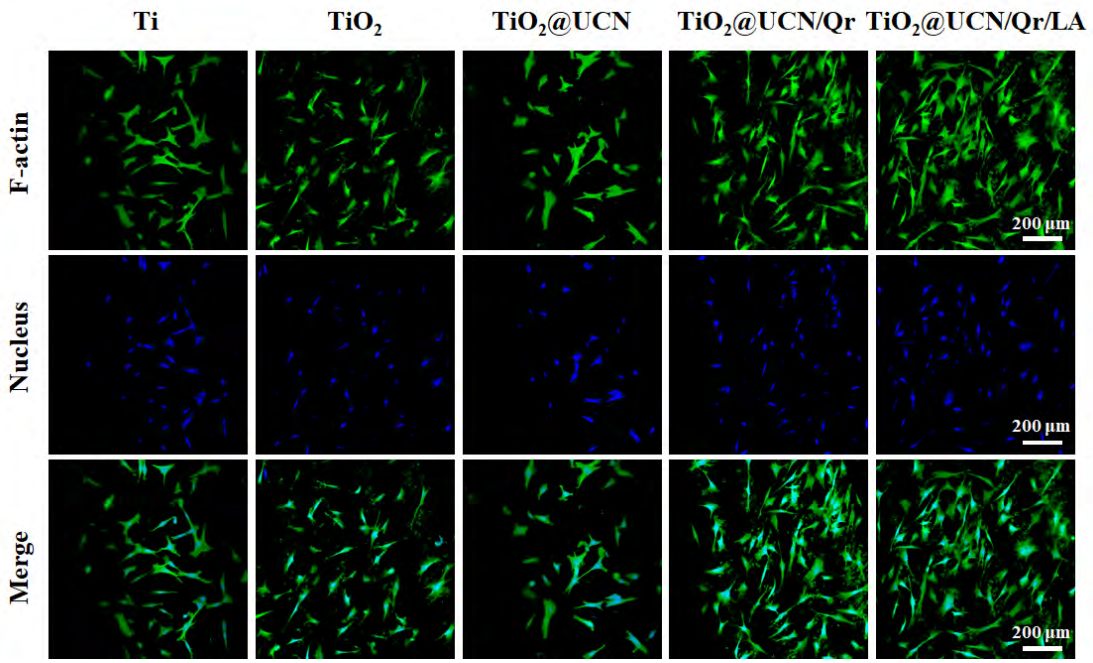

Figure S14. Fluorescence images of BMSCs after culturing for 1 day without 1,060 nm light irradiation.

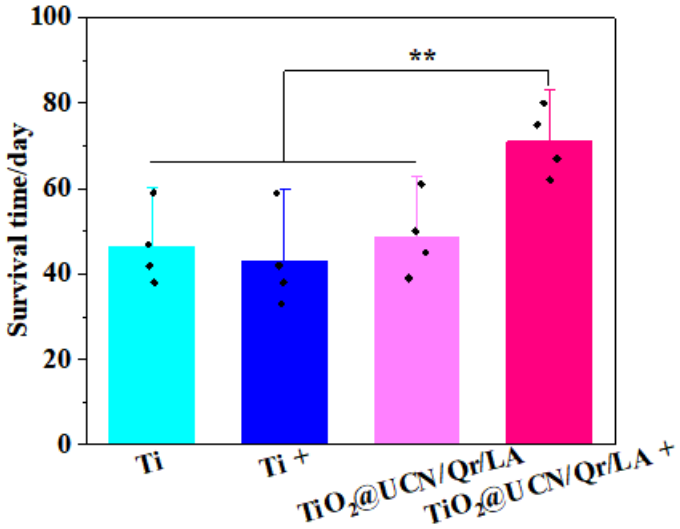

Figure S15. Survival curves of nude mice after different treatments.

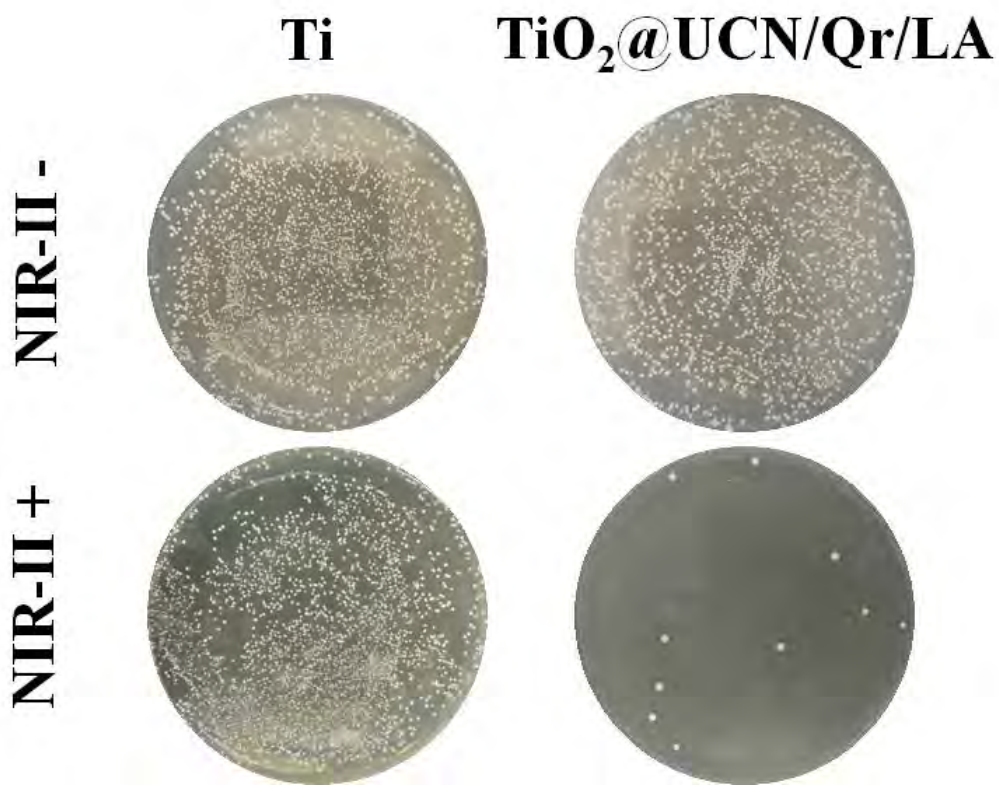

Figure S16. Spread plate results of Ti and TiO_2@UCN/Qr/LA rods with and without 1,060 nm light irradiation obtained from mice.

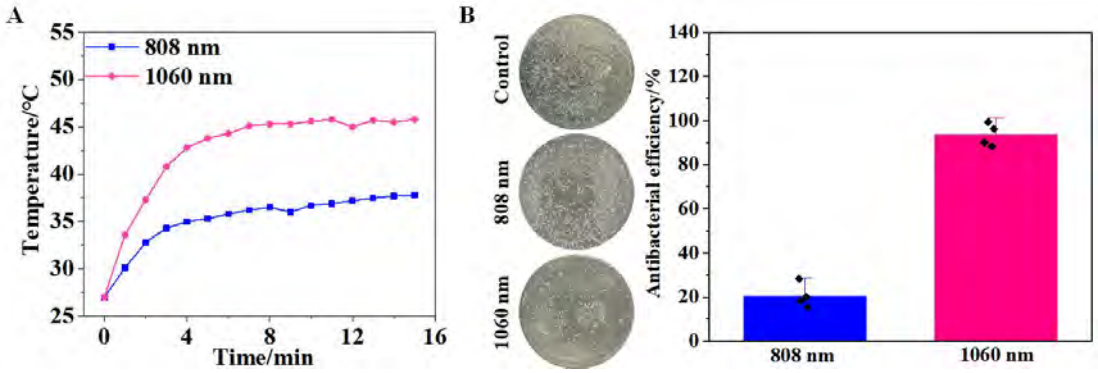

Figure S17. (A) Temperature change curves of TiO_2@UCN/Qr/LA with 808 nm and 1060 nm laser (1 W cm^{-2}) irradiation in rabbit femoral; (B) Spread plate results of TiO_2@UCN/Qr/LA rods upon 808 nm and 1,060 nm laser irradiation for 15 minutes obtained from rabbits.

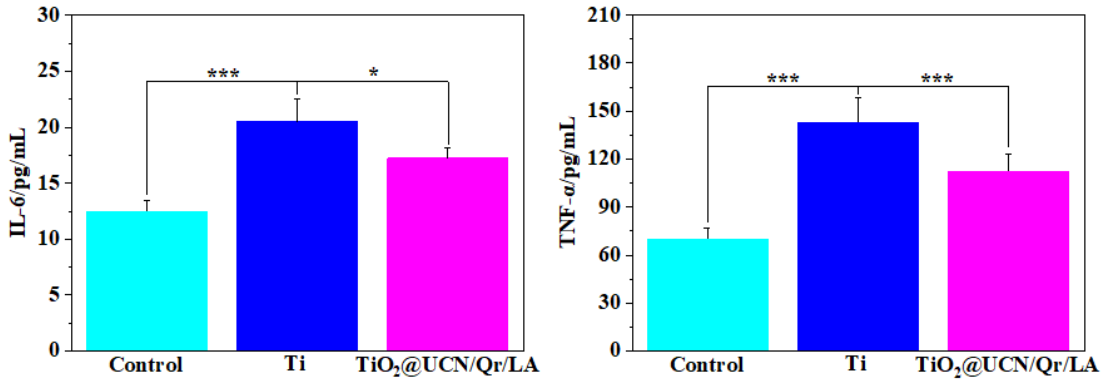

Figure S18. Anti-inflammation evaluation of Ti and TiO_2@UCN/Qr/LA without biofilms *in vitro*.

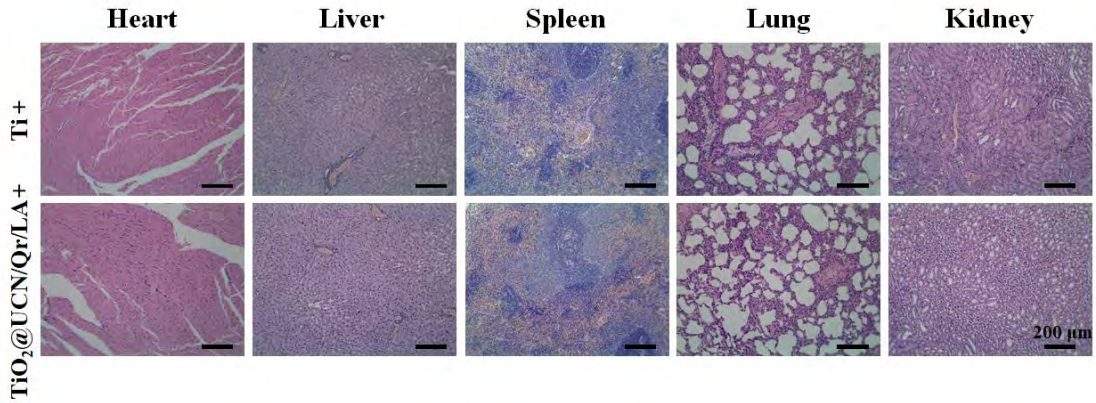

Figure S19. Histological analysis of major organs including the liver, spleen, kidney, heart, and lung by H&E staining.

Table S1. Primer sequences in the real-time polymerase chain reaction (RT-PCR) analysis.

Gene	Gene forward primer sequence (5'–3')	Reverse primer sequence (5'–3')
GAPDH	GGTTGTCTCCTGCGACTTCA	TGGTCCAGGGTTTCTTACTCC
OCN	AGACTCCGGCGCTACCTTGG	CGGTCTTCAAGCCATACTGGTCTG
OPN	ATCTCCTTGCGCCACAGAATGC	ATCTCCTTGCGCCACAGAATGC
RUNX2	AACCCACGAATGCACTACCCA	GGAACTGATAGGATGCTGACGAAG

Table S2. The relative chemical composition (at.%) of the surface elements on TiO_2@UCN, TiO_2@UCN/APTES, TiO_2@UCN/Qr and TiO_2@UCN/Qr/LA detected by XPS.

Samples	Ti 2p (%)	C 1s (%)	N 1s (%)	O 1s (%)	Si 2p (%)	Yb 4d (%)	Er 4d (%)
TiO_2@UCN	1.55	38.95	5.22	50.3	0	1.9	0.8
TiO_2@UCN/APTES	1.04	74.26	3.8	15.74	4.45	0.32	0.11
TiO_2@UCN/Qr	1.15	63.17	4.49	26.99	1.07	0.11	0.02
TiO_2@UCN/Qr/LA	0.62	63.78	17.61	17.49	0.45	0.04	0